11. Photosensitivity in Glasses

Yasuhiko Shimotsuma, Masaaki Sakakura, Masahiro Shimizu, Kiyotaka Miura, Kazuyuki Hirao, Jianrong Qiu, Peter G. Kazansky

A photosensitive glass containing a small amount of a photosensitive metal such as Au, Ag, or Cu, and a sensitizer of CeO_2, is expressed a function of the redox reaction induced by the irradiation of ultraviolet (UV) light. In particular, a photosensitive glass is an indispensable material in the photolithography technique, which is valuable in the microprocessing of glass substrates. Here we aim to discuss the photosensitivity of glass from the perspectives of photochemical, photophysical, and photothermal mechanisms. In particular, from three different points of view (photothermal, photochemical, and photophysical interactions), various intriguing phenomena induced by ultrashort pulse lasers are addressed. Furthermore, a new type of photosensitivity exhibiting nonreciprocal characteristics is also discussed.

The well-cited story of the origin of glass is an episode in the *Natural History* by Pliny of ancient Rome. He wrote a romance-packed story. His unintentional discovery story is as follows [11.1]:

> There is a story that once a ship belonging to some traders in natural soda put in here and that they scattered along the shore to prepare a meal. Since, however, no stones suitable for supporting their cauldrons were forthcoming, they rested them on lumps of soda from their cargo. When these became heated and completely mingled with the sand on the beach a strange translucent liquid flowed forth in streams; and this, it is said, was the origin of glass.

Even now, thousands of years later, glass is used in our life. Glass, including stained glass, gives us a beautiful impression of light, but also acts as a functional material with refractory properties, thermal shock resistance, water resistance, and excellent chemical stability. Besides, it is well known that various phenomena associated with a change in optical properties of materials can be caused by external energy. Table 11.1 shows typical physical phenomena that cause changes in optical properties. The changes in refractive index and birefringence basically lead to the control of the polarization characteristics. If these changes are large, the reflection characteristics are also changed. In addition, the light scattering phenomenon can occur according to the shape of the material, while the changes in the absorption coefficient are directly reflected in the absorption characteristics of the materials.

Even now many studies are performed using such interesting phenomena induced by external fields. In particular, photosensitive glass is one of the key ma-

J.D. Musgraves, J. Hu, L. Calvez (Eds.), *Springer Handbook of Glass*, Springer Handbooks,
https://doi.org/10.1007/978-3-319-93728-1_11

Table 11.1 Typical physical phenomena that cause changes in optical properties

External energy		Refractive index	Absorption	Reflection
Electric field	Field	Pockels effect Kerr effect	Franz–Keldysh effect Kern–Harbeke effect	
	Current		Electrochromism	Drude reflection
Magnetic field		Cotton–Mouton effect Faraday effect		Magneto-optic Kerr effect
Acoustic field		Photoelasticity Acousto-optic effect		Piezoreflectance
Photon			Photochromism	
Thermal		Thermochromism	Thermochromism	Thermochromism

terials used to achieve the printing and reproducing processes. Such a technique is suggestive of a *photographic plate* consisting of a glass plate covered by the light-sensitive emulsion of silver salts. In 1937, R. H. Dalton at Corning Glass Works found that certain copper-containing glasses, when exposed to ultraviolet light, would develop a more intense red color on subsequent heat treatment than that produced in unexposed glass. A few years later, in 1941, S. D. Stookey deduced that the effect produced by ultraviolet exposure and heat treatment was very sensitive to the oxidation state of the copper in the glass and also showed that the process was actually a combination of photochemical and thermal reduction of cuprous ions to colloidal copper [11.2]. He also found that gold and silver are better photosensitive agents than copper and that cerium acts as a sensitizer material [11.3]. *W. H. Armistead* also proposed silver-containing photosensitive glasses [11.4]. Such photosensitive glass typically includes chemical components that cause the coloring and the opaque crystallization by using UV light or x-ray irradiation and the successive thermal treatment. Typical mechanisms of photosensitivity are interpreted as follows: when the photons such as in UV light or x-rays are irradiated, a portion of the electrons excited from the sensitizer (e. g., Ce^{3+} ions) is trapped by the photosensitive metal ions, and then the metal ions are reduced to metal atoms (e. g., Au, Ag, and Cu)

$$Ce^{3+} + h\nu \rightarrow Ce^{4+} \quad (11.1)$$

$$M^{+} + e^{-} \rightarrow M^{0} \text{ (M: Au, Ag, and Cu)} \quad (11.2)$$

Further thermal treatment promotes aggregation of metal atoms to colloids

$$nM^{0} \rightarrow M_{n}^{0} \quad (11.3)$$

For example, in the case of the partial crystallization of glass composed of a Li_2O-SiO_2 system, since such colloids act as the crystal nuclei [11.5], the photoirradiated regions are colored. Since an etching rate of Li_2O-SiO_2 crystals in hydrofluoric (HF) acid is significantly higher than that of glass matrices, selective etching is possible in the regions where Li_2O-SiO_2 crystals are grown. Such glass is commonly called *photosensitive machinable glass*. Of course, such photoreduction based on irreversible photoinduced homogeneous nucleation is included in the interactions between light and glass, which have been widely studied in photochromic glass [11.6], polychromatic glass [11.7], and photocatalytic glass [11.8]. In recent years, the studies of photosensitive glass, such as the writing of a Bragg grating into an optical fiber [11.9–14] and the persistent spectral hole burning in glass [11.15–19] have been pursued both in respect to understanding the mechanisms and applying them to new devices. These reactions are basically realized by the various photoinduced structural changes as a result of the optical absorption of the glass. Therefore, since the excited photoreaction is more active in the vicinity of the glass surface, it is more difficult to induce directly inside a material. The excitation is generally performed by using a laser source in the ultraviolet or visible region owing to its high temporal and spatial coherence [11.20–23]. It is difficult to react the glass with a laser beam with a wavelength that is not in the photon absorption region of the glass. On the other hand, by using a subpicosecond pulse width laser beam, even if its wavelength is not resonant with a glass, it becomes possible to cause various interactions based on the nonlinear optical phenomena [11.24]. Recent progress in producing intense ultrashort laser pulses [11.25, 26] not only pushes the photosensitive glass technologies towards the next stage, but it also opens the door to precise and efficient direct-writing inside glass. The light-matter interactions using ultrashort pulses provide many advantages including resistless and maskless pattering, high flexibility, and high speed machining, compared to other sources of UV light or longer pulse lasers [11.27]. In particular, recent ultrashort pulse laser sources with an average power in excess of 10 W [11.28] have become commercially available and widely used in the field of material processing. From the viewpoint of photosensitive glass technologies, this chapter is focused on various interactions between the material and the ultrashort laser pulses.

11.1 Photothermal Interaction in Glass

11.1.1 Suppression of Thermal Effects

In general, when considering light-matter interactions, the material firstly absorbs a photon. In the case of transparent materials such as glass, the excitation of electrons from the valence band to the conduction band is initiated through nonlinear processes such as multiphoton or tunnel ionization [11.29, 30]. The electrons can then further absorb the photon via the inverse bremsstrahlung process leading to electron heating or avalanche ionization. Although this situation can also be achieved by nanosecond lasers, in this case the initial electrons are mainly generated by the contribution of defects and impurities [11.27]. The fluctuation associated with the optical breakdown threshold can be reduced by employing ultrashort lasers, which results in high reproducibility and controllability [11.31, 32]. Since pulse width is shorter than the electron–phonon coupling time (in the order of ps), the laser energy can be injected into the material before the thermal diffusion occurs [11.29, 32]. Since it is easy to achieve the power density over $\mathrm{TW/cm^2}$ by a condensing lens, the above-mentioned nonlinear optical effects can be space-selectively induced in the vicinity of the focus point [11.29, 33].

Based on the timescales of various electron and lattice processes in laser-excited solids (Fig. 11.1) [11.34], it is clear that the transition into the thermal process occurs on the order of picoseconds. This is the border between thermal and nonthermal processing. Thermal diffusion length (L_{th}) is defined by the pulse width and the thermal diffusion coefficient of the material as follows

$$L_{\mathrm{th}} = \sqrt{2\kappa\tau_{\mathrm{p}}}\,, \tag{11.4}$$

where κ ($= \alpha_{\mathrm{t}}\rho c_{\mathrm{p}}$) is the thermal conductivity obtained by the thermal diffusivity α_{t}, the specific heat c_{p}, and the density ρ, and τ_{p} is the pulse width. Assuming the electron–phonon coupling time is 1 ps, the L_{th} is considered to be about 10 nm at the boundary between thermal and nonthermal processing. Since the pulse width is shorter than a typical thermal relaxation time, more precise calculation using a two-temperature model should be required. Thus, the photoinduced reaction by the single femtosecond pulse or the low pulse repetition rate is considered to proceed in the nonthermal process. Since the thermal accumulation can occur according to multiple-pulse irradiation, it is also possible to control the thermal effect [11.35].

11.1.2 Material Modification

The propagation of intense ultrashort laser pulses in transparent materials causes not only linear effects including diffraction, dispersion, and aberration, but also nonlinear effects such as self-focusing, filamentation, and plasma defocusing [11.36]. The strength of such effects depends on the experimental conditions and the laser parameters. The synergetic contribution of these nonlinear effects and the suppression of thermal effects produces unique subdiffraction-limited processing at an arbitrary location in the material. The intensity distribution in the focal spot of the ultrashort laser pulse will

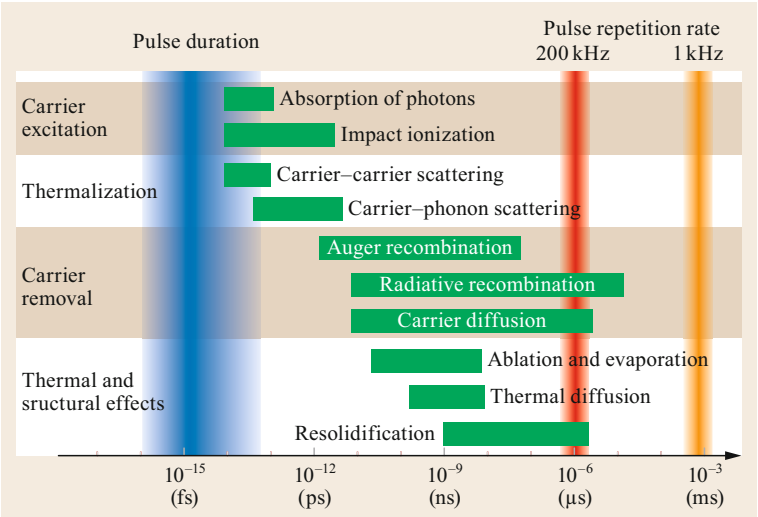

Fig. 11.1 Timescales of various electron and lattice processes in laser-excited solids. Figure was rearranged on the basis of [11.34]

ideally have a Gaussian spatial profile. Thus, the modified region can be limited to only the central area of the focal spot by adjusting the laser intensity to match the threshold intensity (Fig. 11.2a). By adjusting the laser intensity corresponding to the threshold intensity for a reaction (Fig. 11.2b), in principle, the diffraction limit does not put any constraint on the fabrication resolution. Assuming that thermal diffusion in ultrashort laser processing is negligible, the combination of the high numerical aperture (NA) objective and the multiphoton absorption effect enables subwavelength fabrication resolutions beyond the diffraction limit of light [11.37].

However, in practice, the deterioration of the intensity distribution at the focus point also occurs. Since many articles relating to such nonlinear effects including self-focusing have been published [11.38], here we focus on the spherical aberration owing to refractive index mismatch. Indeed, spherical aberrations influence the propagation of ultrashort pulses inside a material, leading to the elongation of the modified region in the direction of the laser propagation [11.39]. To interpret experiments with the presence of refractive index mismatch, the electric field distributions near the focus of an objective with NA inside a material (refractive index:

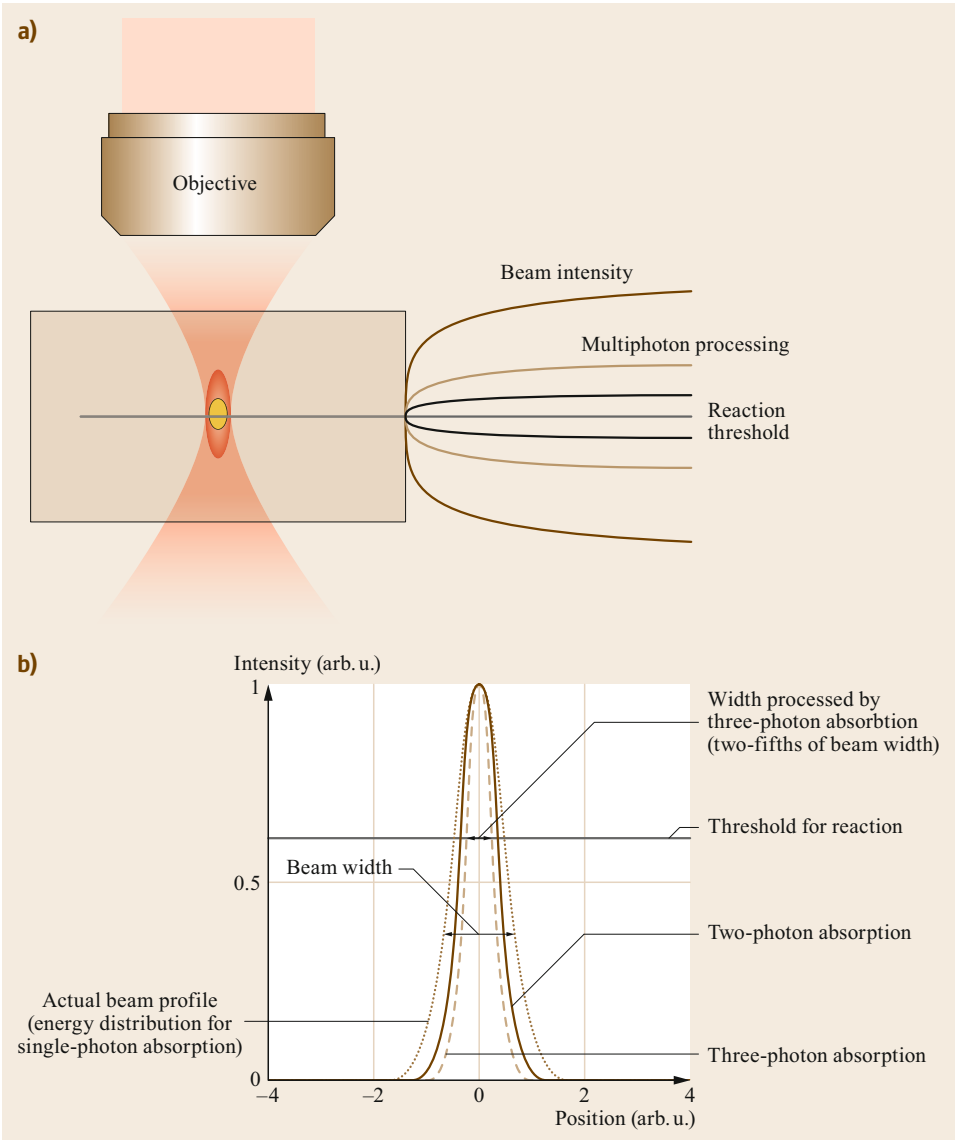

Fig. 11.2 **(a)** Schematic illustration of subdiffraction-limited processing based on multiphoton absorption. **(b)** Beam profile (*dotted line*) and spatial distributions of laser energy absorbed by materials via two- (*solid line*) and three-photon (*line*) absorption. The solid horizontal line indicates the reaction threshold. After [11.27]

n_2) can be expressed as [11.40]

$$E(r,z) = \int_0^{\phi} \sqrt{\cos\varphi_1}\sin\varphi_1(\tau_s + \tau_p\cos\varphi_2) \times J_0(k_0 r n_1 \sin\varphi_1) \times \exp(i\Phi + ik_0 z n_2\cos\varphi_2)\mathrm{d}\varphi_1 \,, \quad (11.5)$$

where $\phi = \sin^{-1}(\mathrm{NA})$ is the half-angle of the light convergence cone, $k_0 = 2\pi/\lambda$ is the wave number in a vacuum, $r = \sqrt{x^2 + y^2}$ is the radial coordinate, and φ_1 and φ_1 are the angles of the incident and refracted ray respectively, which are related to each other through Snell's law,

$$\varphi_2 = \sin^{-1}\left(\frac{n_1}{n_2}\sin\varphi_1\right). \quad (11.6)$$

The coefficients t_s and t_p are the Fresnel transmission coefficients for s and p polarizations

$$t_s = \frac{2\sin\varphi_2\cos\varphi_1}{\sin(\varphi_1+\varphi_2)}\,, \quad (11.7)$$

$$t_p = \frac{2\sin\varphi_2\cos\varphi_1}{\sin(\varphi_1+\varphi_2)\sin(\varphi_1-\varphi_2)}\,. \quad (11.8)$$

J_0 is the zero-order Bessel function. The function is the spherical aberration function caused by the mismatching of the refractive indices [11.42]

$$\Phi = -k_0 d(n_1\cos\varphi_1 - n_2\cos\varphi_2)\,, \quad (11.9)$$

where d represents the distance between sample surface and geometrical focus. This term linearly increases with the distance of d, leading to the increase of the laser-induced damage threshold, owing to the spreading of the laser energy along the laser propagation direction [11.40].

11.1.3 Thermal Accumulation

Figure 11.3a shows the shape changes in the photoinduced structures depending on the pulse repetition rate (R_{rate}) [11.41]. For lower R_{rate} than the thermal diffusion timescale (e. g., 1 kHz), it is considered that heat accumulation does not occur in the photoexcited region. Therefore, even though the temperature elevation is more than several thousand degrees higher at the focus, the localized structural changes such as a defect formation are observed only in a laser focal region [11.43, 44]. Such a phenomenon is due to the thermal energy diffusion out of the photoexcited region during the interpulse time (Fig. 11.3b). On the other hand, when heat accumulation occurs by irradiation at 250 kHz, the modification volume is much

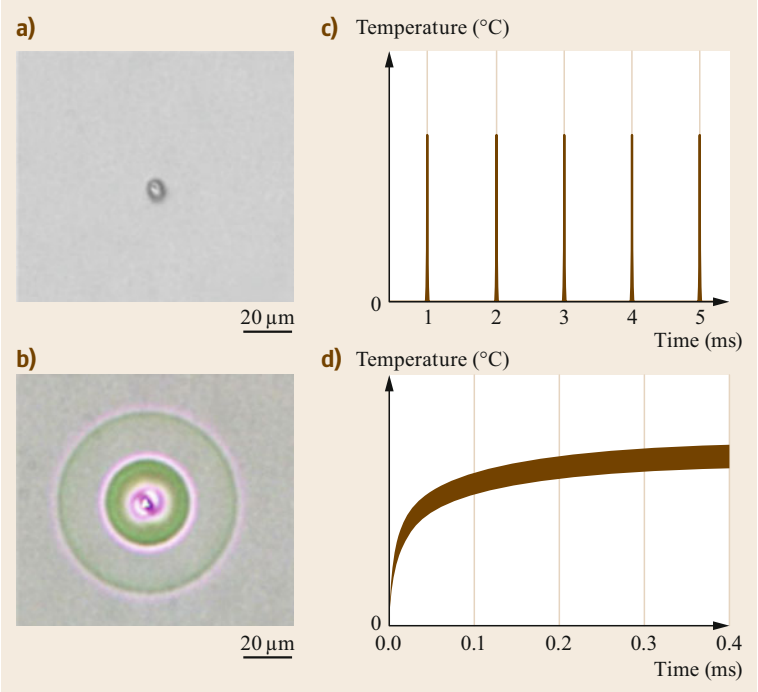

Fig. 11.3a–d Optical microscope images of photoinduced structures by femtosecond laser irradiation at **(a)** 1 kHz and **(b)** 250 kHz. Time profiles of the simulated temperature at the focus for **(c)** 1 kHz and **(d)** 250 kHz. The pulse energy was 2.0 J in both cases. Reprinted from [11.41] with the permission of AIP Publishing

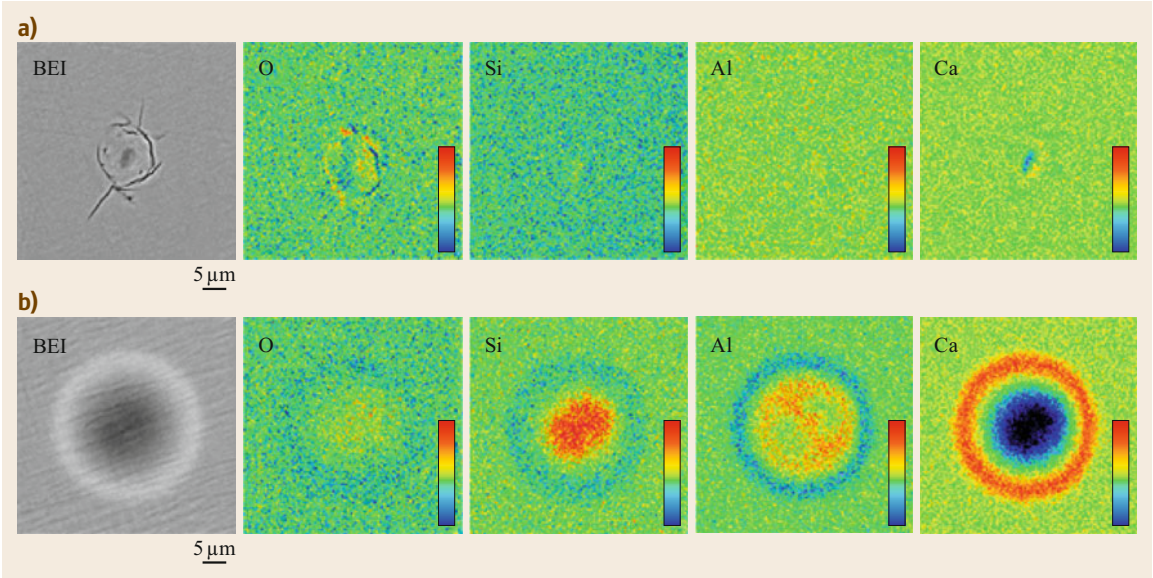

Fig. 11.4a,b BEIs and element maps on a CSA glass surface polished to the depth of focal spot location of the femtosecond laser pulses. The laser parameters are **(a)** 4.27×10^3 J/cm^2 at 1 kHz and (b) 8.12×10^1 J/cm^2 at 200 kHz. Reprinted with permission from [11.47]

larger compared to that for 1 kHz (Fig. 11.3c). When the multiple pulses are focused at a high R_{rate}, the following pulse excites the photoexcited region before heat diffuses out, resulting in a larger heat-affected zone (Fig. 11.3d). *S. M. Eaton* et al. have also observed cumulative heating during direct waveguide writing in glass using a high R_{rate} femtosecond laser [11.45, 46]. Typically, two boundaries are concentric-circularly observed around the photoexcited region (Fig. 11.3c). The formation of the outermost boundary can be explained by a viscoelastic model [11.35]. On the other hand, during the laser irradiation, convection of material was observed in the region inside the inner boundary. As a result, interesting phenomena ranging from the precipitation of crystals [11.48], the material composition change [11.49, 50], to the phase separation [11.47], occur in this region.

11.1.4 Element Migration

Element migration and phase separation inside the inner boundary can be space-selectively induced by femtosecond laser pulses with high R_{rate} [11.47]. Since the interpulse time at 200 kHz ($\tau_{int} = 5\,\mu$s) is much shorter than the thermal diffusion obtained by (11.4), the photoinduced structure in a glass sample is affected by the thermal accumulation. Figure 11.4 shows backscattering electron images (BEIs) and electron probe x-ray microanalysis (EPMA) spectra maps on the glass surface polished to the depth of focal spot location. Typical

Table 11.2 Composition of calcium aluminosilicate glass (mol%)

Glass sample	CaO	SiO_2	Al
CSA	40	40	20

calcium aluminosilicate (CSA) glass was used in the experiments [11.47]. The glass composition is shown in Table 11.2. We have evaluated the difference in element migration induced by femtosecond laser pulses with the different R_{rate}. The laser fluence was 4.27×10^3 J/cm^2 at 1 kHz and 8.12×10^1 J/cm^2 at 200 kHz. Laser writing with a speed of 50 μm/s was performed in the parallel direction to the optical axis from bottom to top surface.

In the case of $R_{rate} = 200$ kHz, the heat was diffused only $\approx 2\,\mu$m during the τ_{int} of 5 μs. Meanwhile, in the case of 1 kHz ($\tau_{int} = 1$ ms), the heat already diffused away from the focal spot to $\approx 30\,\mu$m before the arrival of the next pulse [11.47]. It is known that modifying ions such as Ca^{2+} and Na^+ in a glass matrix can migrate according to a temperature gradient. Indeed, for the 200 kHz case, Ca concentration was decreased (increased) in the center (surrounding) area of the photoexcited region, while Si was concentrated in the center part due to its characteristic strong network former properties (Fig. 11.4b). On the other hand, no apparent element migration was observed in the case of 1 kHz (Fig. 11.4a). We have confirmed that the temperature at the focus exceeds 1000 °C just after the laser irradiation and a temperature gradient over several tens

of °C/m was formed throughout the inner boundary corresponding to the element migration region. Therefore, this element migration phenomenon might largely be due to thermomigration (Soret effect) [11.51]. The iteration of the thermal expansion and the pressure wave originating from pulse-to-pulse temperature elevation may also be related to this phenomenon [11.52].

11.1.5 Phase Separation

Space-selective phase separation can be successfully induced inside a sodium silicate (Na_2O-SiO_2) glass by changing the local composition from a miscible domain to an immiscible one via femtosecond-pulsed laser irradiation with high R_{rate} [11.53]. Previously, the phase separation of the Na_2O-SiO_2 glass system has been investigated [11.54, 55]. For example, in the case of 12 mol% Na_2O concentration, three behaviors were noted depending on the heat-treatment temperatures: spinodal dome for temperatures below 700 °C, immiscibility dome for treatments between 700 and 775 °C, and miscibility region above 800 °C, in agreement with the phase diagram of the Na_2O-SiO_2 system reported by *Haller* et al. [11.56] and shown in Fig. 11.5.

To test the phase separation of the Na_2O-SiO_2 glass system, glass samples with Na_2O concentrations from 21 to 30 mol% were prepared. Femtosecond laser pulses operating at 250 kHz (τ_p: 80 fs, λ: 800 nm, τ_{int}: 4 µs) were irradiated inside a glass sample via objective lens (20×, NA0.45). The pulse energy was tuned to be 3 µJ by the neutral density filter. After the laser irradiation, the glass samples were heat treated at 575 °C. At this temperature, the initial compositions lie outside the immiscible region. The distribution of the Na_2O concentration in the photoexcited region was estimated by the peak shift of the Raman band (Fig. 11.6). The Na_2O concentration at the center part increased approximately 10 mol% compared to the initial concentration, while the concentration at the region approximately 30 µm away from the center slightly increased. This composition change means that Na_2O migrated toward the outside and SiO_2 migrated toward the center during laser irradiation. Consequently, since the glass composition was changed space-selectively from the immiscible region to the miscible, the laser-induced element migration leads to local phase separation.

Figure 11.7 shows scanning electron microscope (SEM) images of the photoexcited region in the 26 mol% Na_2O glass sample. After laser irradiation, the glass sample was treated with heat at 575 °C, and then polished to the depth of focal location. The observation surface was also etched with HF solution. A granular surface was observed after 3 h of heat treatment, suggesting that the relative volume fraction of the Na_2O-rich phase was sufficient for the phase separation (Fig. 11.7c). For heat treatment than longer 12 h, a cocontinuous structure was observed (Fig. 11.7d,e). In particular, pore size between the phase separated structures increased with increasing heat treatment time. It is known that the pore size and specific surface area are

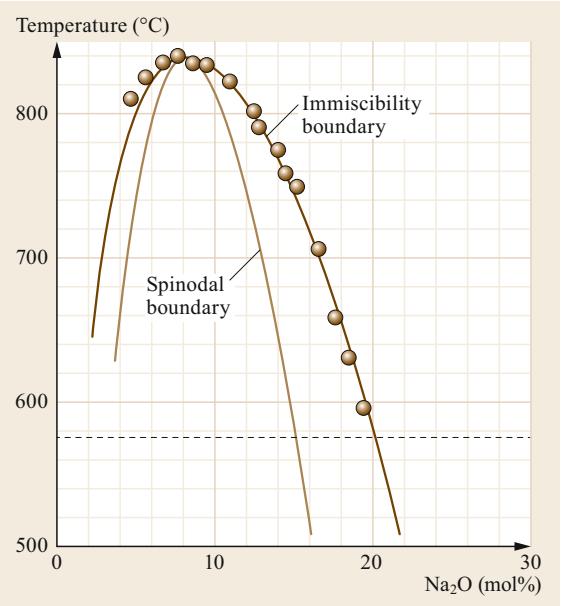

Fig. 11.5 Metastable immiscibility diagram for the Na_2O-SiO_2 system from data of [11.56]. The *dashed line* indicates the heat-treated temperature at 575 °C

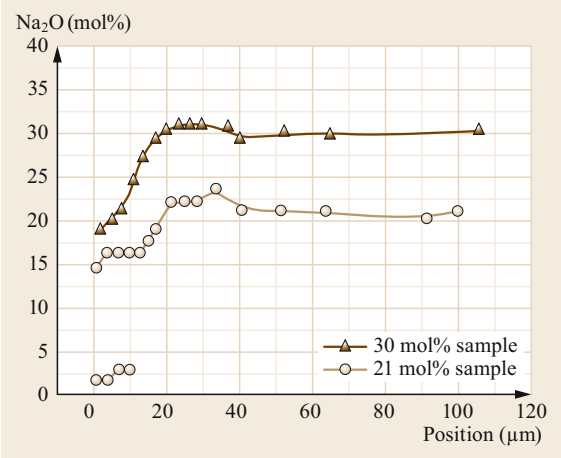

Fig. 11.6 Profiles of Na_2O concentration as a function of the distance from the center of focus area. It should be noted that in the case of the 21 mol% sample, the Na_2O concentration was separated into two at around the center. After [11.53]

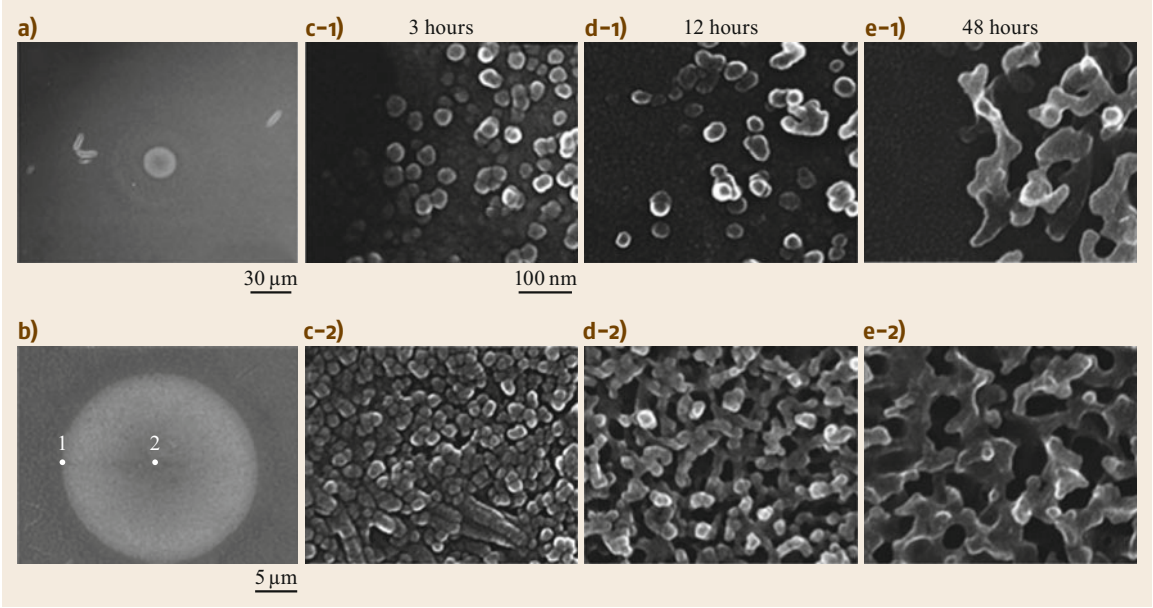

Fig. 11.7a–e SEIs on the surface of the 26 mol% Na_2O sample polished to the depth of focal spot location and etched with HF solution. **(a)** Low magnification SEI, and **(b)** high magnification SEI at around the center of **(a)**. High magnification SEIs for heat-treatment times of **(c)** 3 h, **(d)** 12 h, and **(e)** 48 h. The numbers 1 and 2 correspond to the locations in **(b)**. The magnifications in **(c–e)** are the same. With permission of Springer from [11.53]

proportional to the heat-treatment time [11.57]. These results suggest that the pore size and specific surface area are tunable.

11.1.6 Partial Crystallization

According to the effect of the thermal accumulation, the precipitation of functional crystals inside glass can be realized. In experiments, typical zinc-tellurite (ZT) and niobium-tellurite (NT) glasses have been used [11.58]. Each glass composition is shown in Table 11.3.

The BEIs and the EPMA element maps of the photoexcited region in ZT and NT glass samples are shown in Fig. 11.8. The observation was performed after polishing to the depth of the focus location. It is known that the thermal diffusivity of tellurite glass is typically $\approx 5\times10^{-7}\,m^2/s$. Therefore, temperature at the photoexcited region is increased by the irradiation of laser pulses with the τ_{int} of 5 µs. In the case of the ZT glass sample, Zn concentration at the center part decreased, while Te concentration increased, corresponding to the brighter contrast in BEIs (Fig. 11.8a). The cracks surrounding the modified region could be due to sample polishing. Meanwhile, no apparent migration of oxygen was observed. Although *Nukui* et al. reported crystallization of α-TeO_2 and $Zn_2Te_3O_8$ in zinc-tellurite glass at high temperatures ($\approx 900\,°C$) [11.59], such crystallization has not been observed in our experiments. We assumed that higher temperature and/or longer laser irradiation time were required to precipitate crystals, despite the TeO_2 rich region formed in the center of the focal volume. On the other hand, in the case of the NT glass sample, phase separation into two compounds of Te- or Nb-rich phases were observed. In particular, the shape of the Nb-rich region was a needle-like structure (Fig. 11.8b). It should be noted that the crystalline solid solution of $Nb_2Te_4O_{13}$ ($Nb_2O_5 + 4TeO_2$) is precipitated for the NT glass with higher Nb_2O_5 concentration [11.60].

Table 11.3 Compositions of tellurite glasses (mol%)

Glass sample	ZnO	Nb_2O_5	TeO_2
ZT	20	–	80
NT	–	15	85

11.1.7 Ferroelectric Single-Crystal Waveguide

We have also demonstrated local crystallization in glass induced by femtosecond laser irradiation. The three-dimensional (3-D) waveguides composed of single crystals of $LaBGeO_5$ can be space-selectively written in glass [11.61]. The spherical aberration due to varying the focal spot location inside the material can be dynamically compensated for by switching a hologram displayed on the spatial light modulator

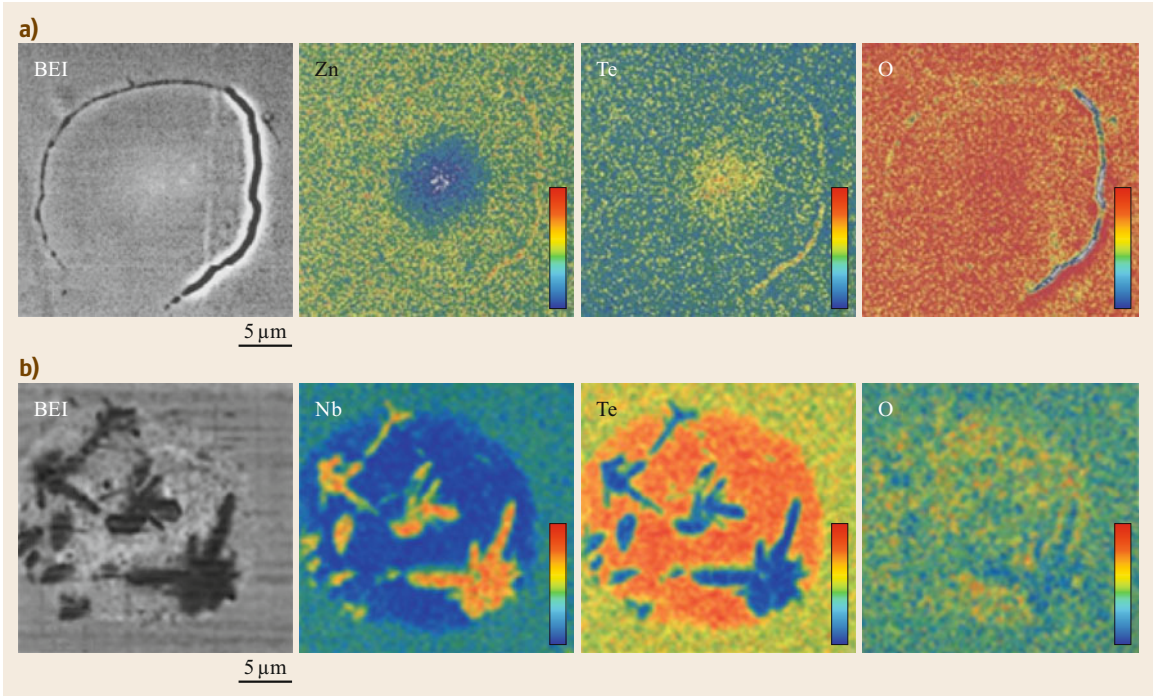

Fig. 11.8a,b BEIs on **(a)** ZT glass and **(b)** NT glass surfaces polished to the depth of focal spot location after 200 kHz repetition rate femtosecond laser pulses irradiation. Reprinted with permission from [11.47]

Fig. 11.9a–d EBSD results for a $LaBGeO_5$ single-crystal track written by femtosecond laser pulses. The laser parameters are as follows: writing speed: 42 µm/s, pulse energy (E_p): 1.2 µJ, pulse repetition rate (R_{rate}): 250 kHz. Spherical aberration correction was performed by SLM. **(a)** Crystal orientation IPF maps, **(b)** color coding corresponding to the crystal orientation parallel to each reference axis, **(c)** illustration of the lattice orientation for a hexagonal crystal, and **(d)** the angular deviations from the average orientation. From [11.61] ►

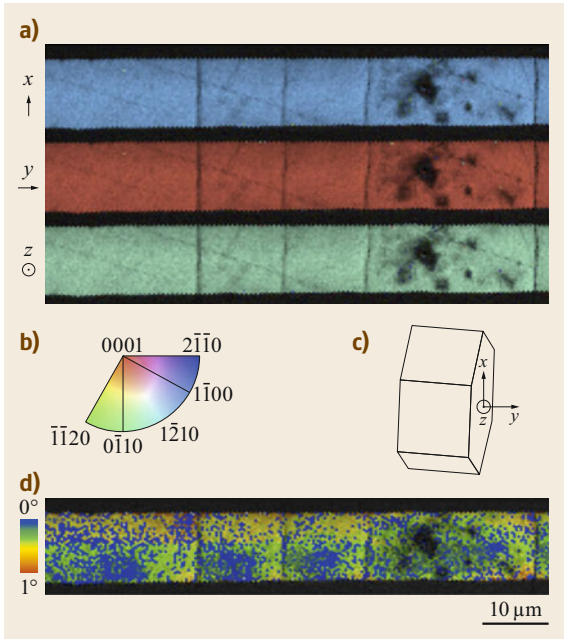

(SLM) [11.62]. Figure 11.9 shows electron backscatter diffraction (EBSD) results for the laser-crystallized track of a ferroelectric $LaBGeO_5$ single crystal. Although faint scratches, surface debris, and transverse cracks due to the polishing were observed, these crystal orientation maps clearly indicate the single hexagonal crystal orientation (Fig. 11.9a–c). To confirm the absence of low-angle grain boundaries, we have also observed the angular misorientations with respect to the average orientation (Fig. 11.9d). This result suggests that the crystal orientation is uniform to within 1°.

11.2 Photochemical Interaction in Glass

11.2.1 Photo-Oxidation of Transition Metal Ions

The space-selective and permanent valence state manipulation of transition and heavy metal ions inside a silicate glass can be successfully induced by focusing femtosecond laser pulses [11.64]. In experiments, Mn and Fe ion codoped silicate glass was used. The glass composition was $70SiO_2$-$20Na_2O$-$10CaO$-$0.1MnO$-$0.05Fe_2O_3$ (mol%). A 4 μm focal spot was formed inside the Mn and Fe ion codoped glass sample by the irradiation of femtosecond laser pulses via 10×, NA 0.30 objective. The laser parameters were as follows: wavelength, λ: 800 nm; pulse width, τ_p: 120 fs; pulse repetition rate, R_{rate}: 1 kHz; pulse energy, E_p: 0.4 mJ; number of pulses, N_{pulse}: 16 pulses. The laser-irradiated area with a diameter of about 30 μm was colored purple. Although the initial glass did not show apparent absorption in the wavelength from 400 to 1000 nm, the increase of the absorption in the wavelength from 300 to 1000 nm was observed at the laser-processed area (Fig. 11.10). The broad peak at 520 nm is assigned to the absorption of Mn^{3+} ions [11.65]. Furthermore, the peak at 320 nm is also assigned to the absorption of hole-trapped centers as observed in the x-ray-irradiated silicate glass [11.66]. It should be noted that Mn^{2+} ions in the initial glass were oxidized to Mn^{3+} by the femtosecond-laser-excited nonlinear optical process. The mechanism of the observed phenomenon have been proposed [11.29]: free electrons are excited via the multiphoton absorption and the following avalanche ionization. Mn^{2+} ions capture a hole resulting in the formation of Mn^{3+} ions, since Fe^{3+} ions, which are also active sites in glass matrix, may act as electron trapping centers. Other mechanisms should also be taken into consideration. It is well known that the filamentation of ultrashort laser pulses is accompanied by the generation of a white-light supercontinuum [11.67]. Since such a white light includes a shorter wavelength component, it is also possible to oxidize Mn^{2+} ions into Mn^{3+}.

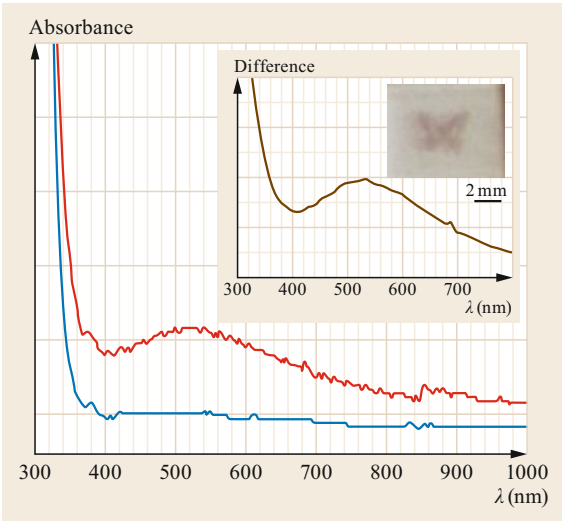

Fig. 11.10 Absorption spectral change of the Mn^{2+} and Fe^{3+} codoped silicate glass by femtosecond laser irradiation (*blue*: before, *red*: after). The *inset* shows the difference in absorption spectrum. A purple butterfly image colored by the laser writing is also shown. After [11.63]. Copyright 2005 The Japan Society of Applied Physics

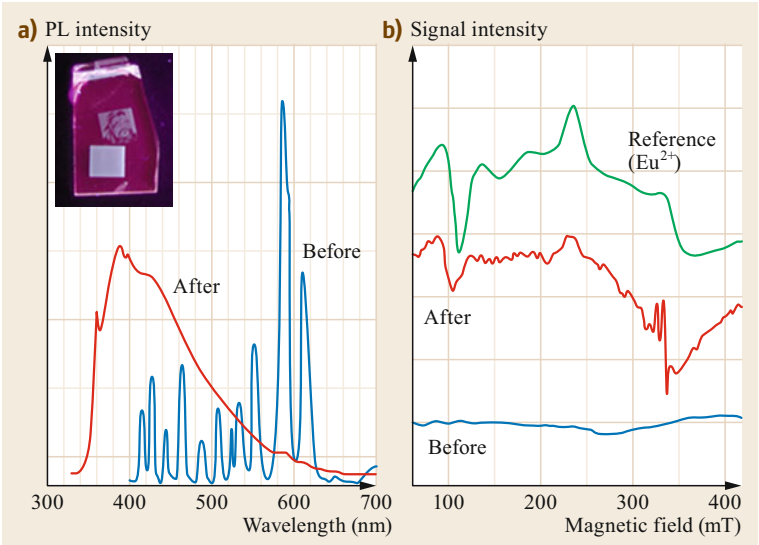

Fig. 11.11 **(a)** Photoluminescence (PL) spectral change of Eu^{3+}-doped fluorozirconate glass by femtosecond laser irradiation (*blue*: before, *red*: after). *Inset* shows the picture that emerged in the Eu^{3+}-doped fluorozirconate glass by laser writing under UV illumination of 365 nm. **(b)** ESR spectra of Eu^{3+}-doped fluorozirconate glass before (*blue*) and after (*red*) femtosecond laser irradiation. A reference ESR spectrum for Eu^{2+}-doped fluoroaluminate glass fabricated in a reducing atmosphere is also shown (*green*). After [11.63]. Copyright 2005 The Japan Society of Applied Physics

11.2.2 Photoreduction of Rare-Earth Ions

The reduction reaction of rare-earth ions in fluoride glass can also be photoinduced by irradiation by the femtosecond laser [11.68]. The Eu^{3+}-doped fluorozirconate glass of $53ZrF_4$-$20NaF$-$20BaF_2$-$3.9LaF_3$-$3AlF_3$-$0.1EuF_3$ (mol%) was used in these experiments. As the reference glass sample, the Eu^{2+}-doped fluoroaluminate glass of $35AlF_3$-$20CaF_3$-$14.9YF_4$-$10MgF_2$-$10SrF_3$-$10BaF_2$-$0.1EuF_2$ was also prepared in a reducing atmosphere. A 10 μm focal spot was formed inside the Eu^{3+}-doped fluorozirconate glass sample by the irradiation of femtosecond laser pulses via 10×, NA 0.30 objective. The laser parameters were as follows: λ: 800 nm, τ_p: 120 fs, R_{rate}: 200 kHz, E_p: 1.0 J, N_{pulse}: 2×10^5 pulses. The photoluminescence (PL) spectra of the Eu^{3+}-doped fluorozirconate glass sample before and after femtosecond laser irradiation are shown in Fig. 11.11a. All PL peaks observed in the initial glass sample can be assigned to the $^5D_0 \rightarrow {}^7F_j$ ($j = 0, 1, 2$) transition of Eu^{3+}. Since Eu ions are present in the trivalent state in the initial glass sample, no apparent emission of Eu^{2+} was detected. After the laser irradiation, the PL peaks at 360 and 400 nm, which are assigned to the $^6P_{7/2} \rightarrow {}^8S_{7/2}$ and $4f^6 5d^1 \rightarrow 4f^7$ transitions of Eu^{2+}, respectively, were observed. To reveal the valence number of Eu in glass, the electron spin resonance (ESR) spectra of the Eu^{3+}-doped fluorozirconate glass sample before and after laser irradiation were measured (Fig. 11.11b). The ESR spectrum of the Eu^{2+}-doped fluoroaluminate glass sample was also shown as reference. Although the initial Eu^{3+}-doped fluorozirconate glass did not show apparent signals, the distinct signals similar to those of the Eu^{2+}-doped fluoroaluminate glass were detected after laser irradiation. Two signals at about 330 mT (splitting coefficient $g \approx 2.0$) can be assigned to hole-trapped V-type centers and to electrons trapped by Zr^{4+} ions [11.70]. These results suggest that some of the Eu^{3+} ions were reduced to Eu^{2+} by femtosecond laser irradiation.

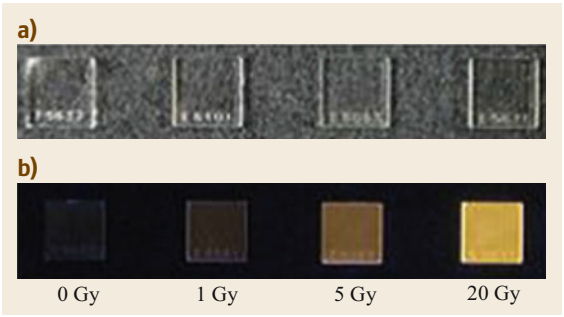

Fig. 11.12a,b Radiophotoluminescence emission images of Ag^+-doped phosphate glass as a function of x-ray absorbed dose: **(a)** under visible light, **(b)** under UV light. Reprinted from [11.69], with permission from Elsevier

11.2.3 Precipitation of Metal Nanoparticles

The photosensitivity of Ag^+-doped phosphate glass is practically used in the individual monitoring of ionizing radiation as well as in monitoring of environmental

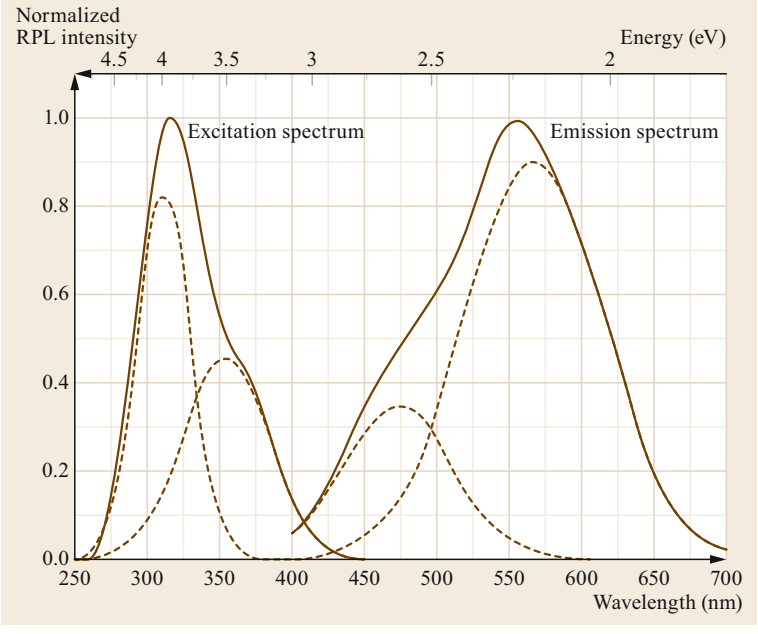

Fig. 11.13 Typical radiophotoluminescence (RPL) emission and excitation spectra of Ag^+-doped phosphate glass after x-ray irradiation. Gaussian peak fitting for RPL emission and excitation spectra are also shown as *dashed lines*. After [11.69]

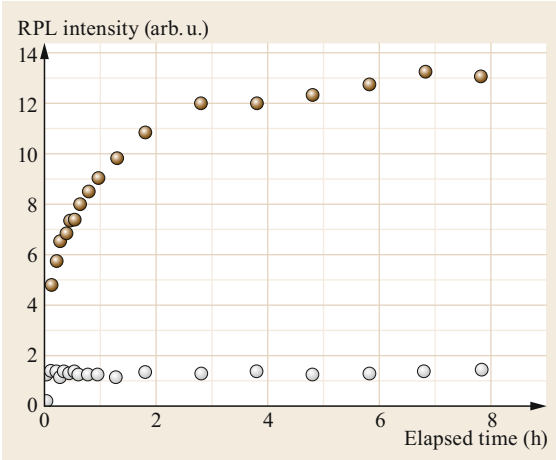

Fig. 11.14 Profiles of RPL emission intensity at 560 nm (*brown circles*) and 460 nm (*gray circles*) as a function of elapsed time. After [11.69]

natural radiation. This phenomenon is based on radiophotoluminescence (RPL). The mechanisms of RPL have been proposed as follows. When the phosphate glass containing Ag^+ ions is exposed to ionizing radiation, the excited electrons are captured into Ag^+ and the valence changes to Ag^0. The holes are also captured by PO_4 tetrahedra, and then Ag^{2+} ions are produced by the interaction between holes and Ag^+ ions. Such Ag^0 and Ag^{2+} ions act as fluorescent centers in the phosphate glass [11.71, 72]. The advantages of such glass dosimeters are: (1) RPL intensity is proportional to the amount of irradiation, and (2) the fluorescence center can be eased by annealing at a high temperature of 400 °C [11.73, 74]. However, details of the mechanisms of the RPL excitation and emission in this glass have not been fully understood. In this section, we discuss the mechanisms of RPL in Ag^+-doped phosphate glass based on the observed phenomena [11.69, 75]. In these experiments, the commercially available Ag^+ doped phosphate glass was used. The photoreduction was performed by the x-rays emitted from an x-ray tube operated at 30 kV and 20 mA, or from femtosecond laser pulses operating at 800 nm (τ_p: 120 fs, R_{rate}: 250 kHz, E_p: 3 μJ) [11.63]. In the case of x-ray irradiation, the orange (yellow + blue) color RPL emission was observed and increased with increasing x-ray absorption dose (Fig. 11.12). This result agreed with that of previous reports [11.76, 77]. Typical RPL emission and its excitation spectra for x-ray-irradiated Ag^+-doped phosphate glass could be fitted to two distinct peaks (Fig. 11.13). The RPL emission and excitation peaks were respectively deconvolved by two peaks of 460 and 560 nm, and 315 and 373 nm. The time decay of the RPL emission intensity of two peaks of 560 nm (yellow) and 460 nm (blue) just after x-ray irradiation is also shown in Fig. 11.14. *Yokota*, *Imagawa* and *Perry* have reported that since many hPO_4 are also photoinduced in the glass matrix, the Ag^{2+} ions are produced by the following reaction [11.76, 78]

$$Ag^+ + hPO_4 \rightarrow Ag^{2+} \,. \qquad (11.10)$$

These results suggest that the yellow RPL emission at 560 nm is attributed to Ag^{2+} ion generation.

Unlike in the x-ray, in the case of femtosecond laser irradiation 20 μm spots with fluorescence peaking at 460 nm were observed (Figs. 11.15 and 11.16). Such a blue RPL emission peak at 460 nm originates from Ag^0 generation in the Ag^+-doped phosphate glass. Indeed, the formation of Ag nanoparticles due to the ag-

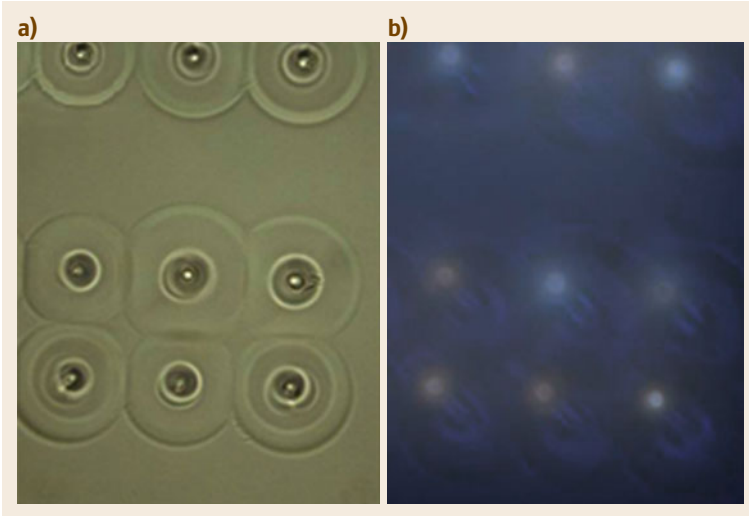

Fig. 11.15a,b Optical microscope images of the photoinduced structures in the Ag^+-doped phosphate glass by femtosecond laser irradiation. Images were taken under visible light **(a)** and UV light **(b)**. Reprinted from [11.69] with permission from Elsevier

gregation of Ag atoms in Ag^+-doped silicate glass by femtosecond laser irradiation and following an annealing process was reported [11.58]. The reason why RPL emission from Ag^0 is dominant for femtosecond laser excitation is considered to be as follows. It is known that the phosphorous-related radiation-induced defects are typically classified into two structures, of phosphorous-oxygen hole centers (POHCs) and phosphorous-oxygen electron centers (POECs) [11.79]. POHCs are hole-trapping defects characterized by an unpaired electron shared by two nonbridging oxygen atoms. POECs consist of unpaired electrons localized on the central P atom in PO_4 tetrahedra. In the case of x-ray, with much shorter wavelength than that for laser light, two such types of defects are induced. On the other hand, electron plasma via multiphoton absorption can be excited by femtosecond laser irradiation. We assumed that the formation of POECs would be suppressed because of the competition between the reduction of Ag^+ ions into Ag^0 and the generation of POECs.

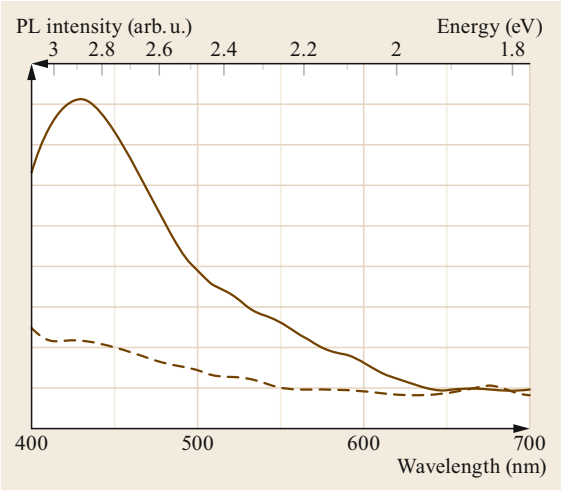

Fig. 11.16 PL spectral change of the Ag^+-doped phosphate glass by femtosecond laser irradiation (*broken line*: before, *solid line*: after). After [11.75]

11.3 Photophysical Interaction in Glass

11.3.1 Classification of Photoinduced Structures in Silica Glass

It is not only photothermal and photochemical modifications inside glass, which are presented in the previous section, that can be induced by ultrashort pulse laser irradiation. In addition, a permanent structural densification of the glass structure can be induced by the irradiation of the intense femtosecond laser pulses, because high-order nonlinear absorption allows energy deposition predominantly within the focal volume [11.80]. Although the process during femtosecond laser interaction with a material is now well investigated, the actual structural changes in various materials are not fully understood [11.81]. According to irradiated femtosecond laser intensity, the photoinduced structures in silica glass can be classified into three different types of modification or damage: a smooth positive refractive-index change due to densification (type-I); optical anisotropy of form birefringence due to self-assembled nanostructure (type-II); and voids and cracks due to Coulomb explosion (type-III) [11.82, 83]. Since the photoexcited region at relatively low laser intensity is homogeneously densified by fast cooling following shockwave generation [11.84, 85], the refractive index is increased (Fig. 11.17).

The type-I modification in refractive index without cracks can be applied to various optical devices such as waveguides and couplers [11.86, 87]. Based on investigations regarding the structural change in silica glass by femtosecond laser irradiation, the densification of the photoexcited region within the focal volume is suggested to be caused by shockwave generation [11.88]. Type-III modification including voids and cracks (Fig. 11.18) has expected applications to data storage and photonic crystals [11.89, 90]. Such destructive modifications of type-III, induced by the higher laser intensity, are derived from an electron-ion plasma through avalanche ionization via inverse bremsstrahlung [11.91, 92].

Permanent birefringence induced by femtosecond laser pulses in fused silica was first observed by *Sudrie* et al. [11.93, 94]. Such optical anisotropy is exhibited by the type-II modification. *Kazansky* et al. have also observed polarization-dependent anisotropic light scattering during femtosecond laser irradiation in Ge-doped silica glass [11.95]. Finally, we have also reported the direct observation of an intermediate type-II structure composed of periodically varying oxygen defect concentration by using electron microscopy [11.96, 97]. These periodic nanostructures with a pitch as small as 200 nm were ruled in the direction parallel to the laser polarization direction (Fig. 11.19). Furthermore, since the concentration of the oxygen defects were periodically changed according to such nanostructures, low refractive index regions i. e., negative birefringence, also periodically appeared in the nanoscale [11.98]. Until now, many types of optical

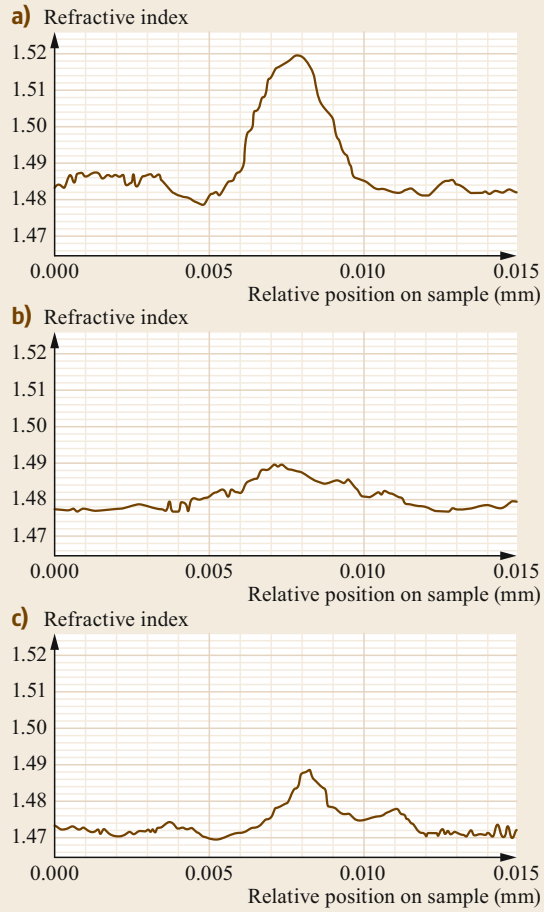

Fig. 11.17a–c Refractive index profiles of the photoinduced structure by femtosecond laser irradiation in **(a,b)** $3GeO_2$-$97SiO_2$ glass and **(c)** pure SiO_2 glass. The laser parameters were as follows: λ: 800 nm, τ_p: 120 fs, R_{rate}: 200 kHz, E_p: 2.35 μJ, writing speed: 100 μm/s, number of scans: **(a,c)** one time, **(b)** 10 times. The refractive indices at near both ends of the profiles correspond to those for the original glass samples. After [11.80]

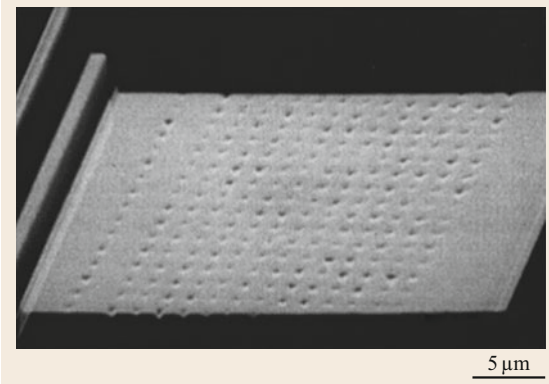

Fig. 11.18 Void array produced by microexplosions inside fused silica. The laser parameters were as follows: λ: 780 nm, τ_p: 100 fs, E_p: 0.5 μJ. Reprinted from [11.85] with permission of AIP Publishing

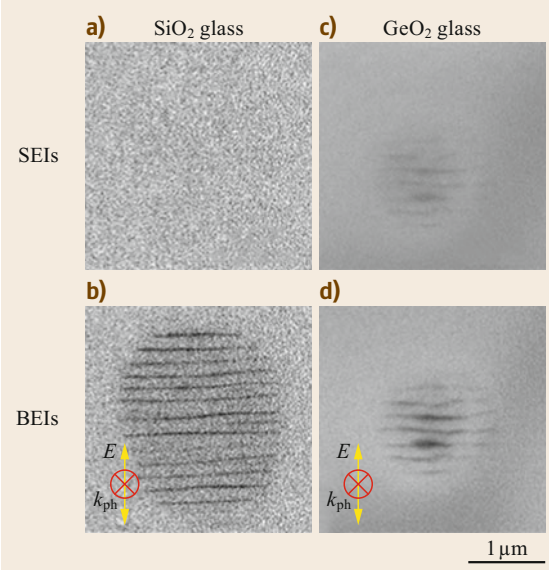

Fig. 11.19a–d Secondary electron images (SEIs) and backscattering electron images (BEIs) of SiO_2 glass **(a,b)** and GeO_2 glass **(c,d)** polished close to the depth of focal spot. k_{ph} and E are the laser propagation direction and the polarization direction, respectively

devices ranging from retardation plates [11.98], microreflectors [11.99], to microfluidic channels [11.100] based on such birefringent nanostructures have been demonstrated. The mechanism for self-assembly of the polarization-dependent periodic nanostructure is, however, still not fully understood [11.101].

11.3.2 Structural Densification (Type-I)

In this section, time-resolved observation of pressure wave generation and propagation are described. This shockwave, resulting from a rapid relaxation of thermoelastic stress, is a possible origin for the photoinduced refractive index change [11.102–104]. It is known that a pure silica (SiO_2) glass exhibits an anomalous behavior in fictive temperature (T_f) [11.105]. T_f is one of the characteristic properties of the glass structure, providing the temperature for reaching a quasi-thermal equilibrium state. Although the density of usual glass is decreased at higher T_f, that of SiO_2 glass is conversely increased with increasing in T_f. Therefore the structure of SiO_2 glass frozen by more rapid cooling be-

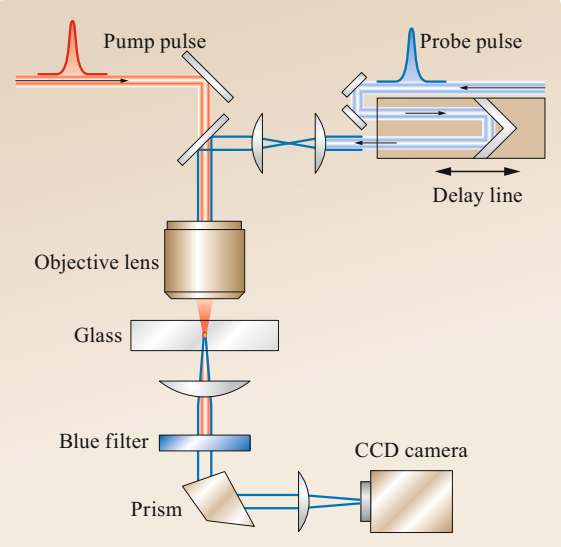

Fig. 11.20 Schematic of experimental system for the TrL method. After [11.88]

comes higher density [11.105, 106]. To reveal the effect of the laser-induced shockwave on the structural modification, we observed a transient lens (TrL) effect by using a pump–probe method. A detailed experimental system for TrL observation (Fig. 11.20) has been reported elsewhere [11.103].

Typical TrL signals obtained by tuning the pump pulse energies are shown in Fig. 11.21a. The negative signal at 0 ps delay time is interpreted in terms of an optical Kerr effect and plasma formation [11.107, 108]. In the case of higher pump pulse energy, the TrL signals clearly oscillated with the passage of delay time. Such oscillation of TrL signals indicates a shockwave generation and propagation [11.103]. Furthermore, the amplitude of the TrL oscillation was increased with increasing pump pulse energy, and we confirmed that the shockwave can be generated by pump pulse energy more than 90 nJ (Fig. 11.21b).

Interestingly, when the pump pulse energy was lower than the threshold of shockwave generation, the TrL signal after the initial response temporarily kept a constant negative value (Fig. 11.22a). This phenomenon is considered to be caused by a refractive index lens effect. In particular, such a positive refractive index change induced by femtosecond laser pulses with a pulse energy lower than the threshold of shockwave generation can also be observed by changing the distance (d) between focal positions of the pump and probe (Fig. 11.22b). The positive (negative) TrL signal in the case of the positive (negative) d clearly indicates that the photoexcited region acts as a convex lens. Such positive refractive index change reached a maximum at the pump pulse energy of about 85 nJ and disappeared below 65 nJ. We speculate that this threshold (≈ 65 nJ) of the transient positive refractive index change is the threshold of the type-I modification in SiO_2 glass.

We have also associated the TrL signals with the structural changes revealed by the Raman measurements (Fig. 11.23a). The measured Raman intensities were subtracted from a luminescence background due to the nonbridging oxygen hole center (NBOHC) at 650 nm [11.109], and corrected for temperature and frequency dependence of the first order (Stokes) Raman scattering [11.110]. Typical Raman peaks at about 450, 490, 600 and 800 cm^{-1} have been identified [11.111, 112]. The 800 cm^{-1} peak has been attributed to the bending vibration of the Si−O bonds. In addition, the sharp Raman peaks at 490 cm^{-1} (D1) and ≈ 600 cm^{-1} (D2) have been respectively attributed to the oxygen

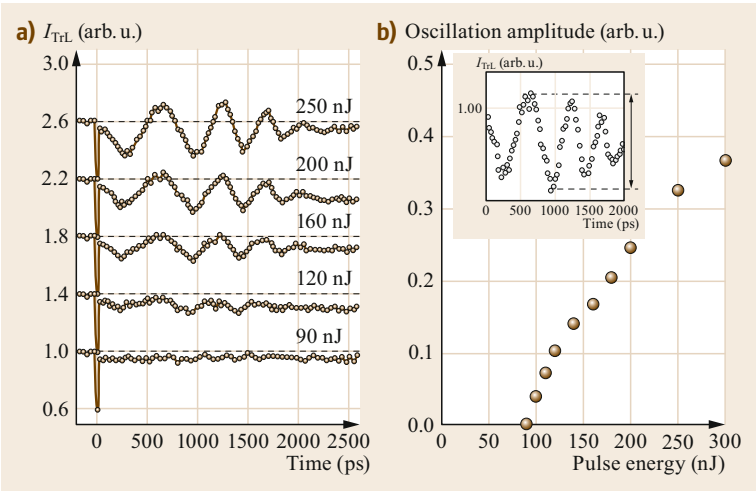

Fig. 11.21 **(a)** TrL signals observed with various pump pulse energies. The baselines for the TrL signals are shown by *dashed lines*. **(b)** Plot of the oscillation amplitude as a function of the pump pulse energy. The oscillation amplitude was defined by the difference in TrL signal intensity between the first positive peak and the second negative peak (*arrow in inset*). After [11.88]

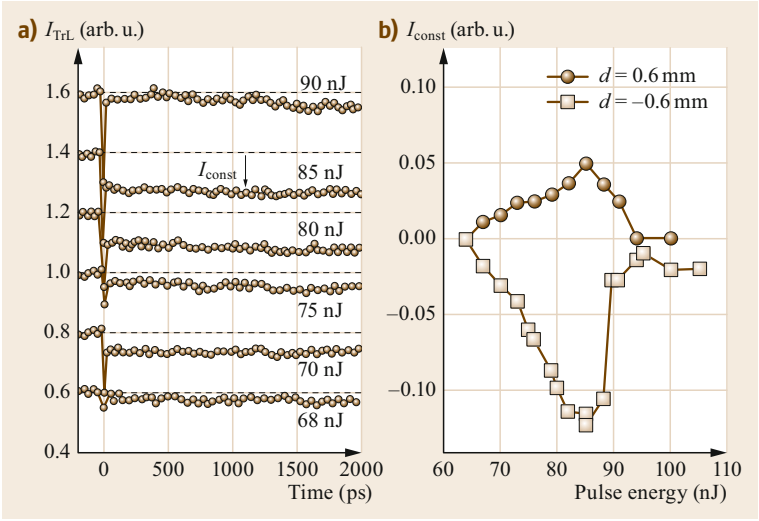

Fig. 11.22 **(a)** TrL signals observed below the pump pulse energy threshold of shockwave generation. **(b)** The temporarily constant intensity (I_{const}) in **(a)** as a function of the pump pulse energy. After [11.88]

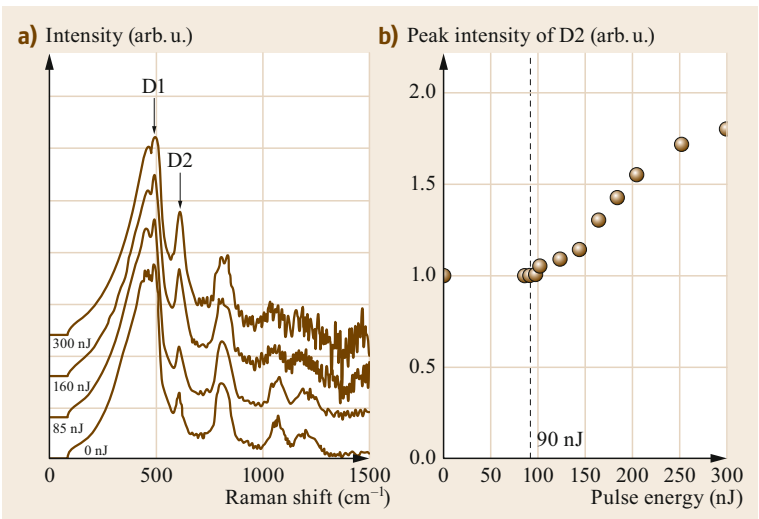

Fig. 11.23 **(a)** Raman spectra of the modified region induced by various pump pulse energies. **(b)** Variation of D2 peak intensity as a function of the pump pulse energy. The intensities were normalized by that of the initial glass. After [11.88]

breathing modes in four- and three-membered rings of SiO_4 tetrahedra. The D2 peak intensity increased with increasing laser pulse energy, which suggests structural densification (Fig. 11.23b). The threshold shown in D2 peak intensity (≈ 90 nJ) was similar to the threshold of shockwave generation (Fig. 11.21b). From the comparison, we suggested that the structural densification according to the formation of the smaller ring structure could be caused by shockwave generation.

We proposed the mechanism of type-I modification in SiO_2 glass based on the elastic deformation [11.102, 113]. The absorbed laser energy via nonlinear optical process is transferred into the lattice system in glass, resulting in temperature elevation. Since this temperature elevation occurs much faster than the elastic deformation [11.108], the thermoelastic stress is concentrated at the photoexcited region. Such stress is relaxed through shockwave generation, followed by structural densification. Although it is not clear whether the generation of the shockwave is triggered by the thermal expansion and/or electron plasma formation, another group has also argues for a cold defect-driven mechanism of densification resulting from defect relaxation [11.114]. The photoinduced shock (i. e., pressure) can also be estimated from the TrL signal fitted by the phase distribution (Fig. 11.24). From the maximum of the phase shift ($\Delta\phi = 0.4$ rad) (Fig. 11.24b), the refractive index change was estimated. The phase shift $\Delta\phi$ is expressed by the formula using the refractive index change Δn

$$\Delta\phi = 2\pi \frac{\Delta n l}{\lambda_{probe}} , \qquad (11.11)$$

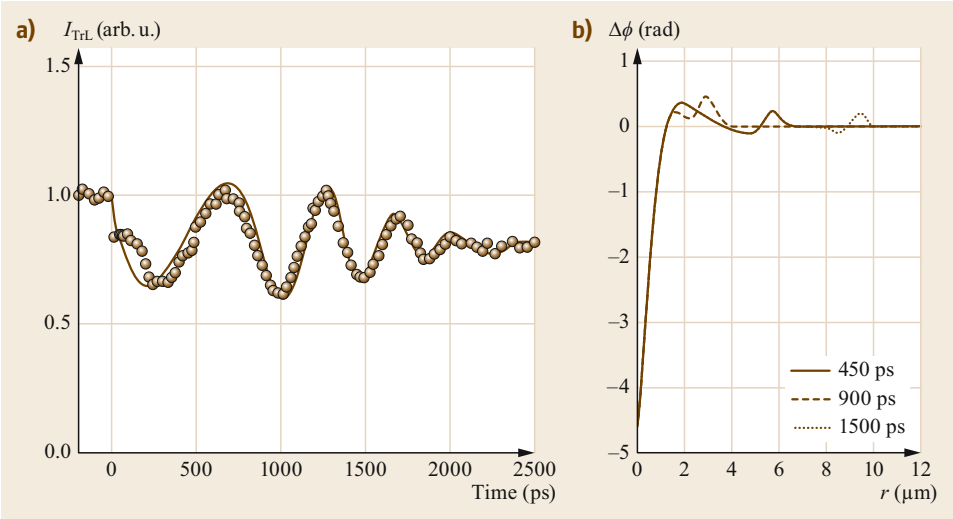

Fig. 11.24 **(a)** TrL signal observed at the pump pulse energy of 300 nJ (*brown circles*). The calculated curve (*solid line*) from the time-dependent phase distribution of the probe pulse is also shown. **(b)** The phase distributions of probe pulses at 450, 900, and 1500 ps. The phase distributions include the contributions from a laser-induced shockwave and the refractive index change in the central region. After [11.88]

where l is the length of the photoexcited region along the laser propagation direction. Assuming the l is 30 μm at 300 nJ, the refractive index change was estimated to be 8.5×10^{-4}. The refractive index change is also expressed by the density change based on the Lorenz–Lorentz relation [11.115]

$$\Delta n = \frac{n_0^4 - 1}{4n_0}\left(\frac{\Delta\rho}{\rho_0}\right), \tag{11.12}$$

where ρ_0 and n_0 are the density and the refractive index of an initial SiO_2 glass respectively. Finally. the following formula is obtained

$$\frac{\Delta\rho}{\rho_0} = \Delta\phi\frac{\lambda_{probe}}{2\pi l}\frac{4n_0}{n_0^4 - 1}\,. \tag{11.13}$$

Using the refractive index of a SiO_2 glass at $\lambda_{probe} = 400$ nm ($n_0 = 1.47$), the density change for $\Delta\phi = 0.4$ rad was estimated to be about 0.14%. Furthermore, the stress associated with the density change is also given by [11.116]

$$\Delta P = K\frac{\Delta\rho}{\rho_0}\,, \tag{11.14}$$

where K is the bulk modulus of a SiO_2 glass (= 37 GPa at 293 K). The maximum stress induced by the shockwave was estimated to be about 50 MPa at 300 nJ. From the thermoelastic simulation, the initial stress induced by the shockwave of 50 MPa in the photoexcited region must be 520 MPa, corresponding to the stress generated by the thermal expansion of 1.4%. Meanwhile, it has been reported that the pressure at the photoexcited region estimated from Raman spectra reaches higher than several GPa [11.112]. This difference suggests that temperature elevation is also related to the structural densification.

11.3.3 Self-Organization of Structural Defects (Type-II)

In addition to the homogeneous densification (type-I modification), the proposed mechanisms of the polarization-dependent self-assembled periodic nanostructure (type-II modification) are discussed in this section. In these experiments, femtosecond laser pulses operating at 250 kHz (τ_p: 80 fs, λ: 800 nm, τ_{int}: 4 μs) were focused via an objective lens (100×, NA 0.80). The depth of focal spot was located approximately 100 μm below the sample surface and then a beam waist diameter was evaluated to be about 1 μm. After laser irradiation, the glass sample was polished to the depth of focal location, then inspected by SEM (Fig. 11.19). It is well known that the surface morphology and the density are reflected in the SEIs and the BEIs respectively. Although slight striation generated during the polishing process was visible on the SEIs of GeO_2 glass, we assumed that no apparent morphological changes such as cracks exist in the focal position for SiO_2 glass and

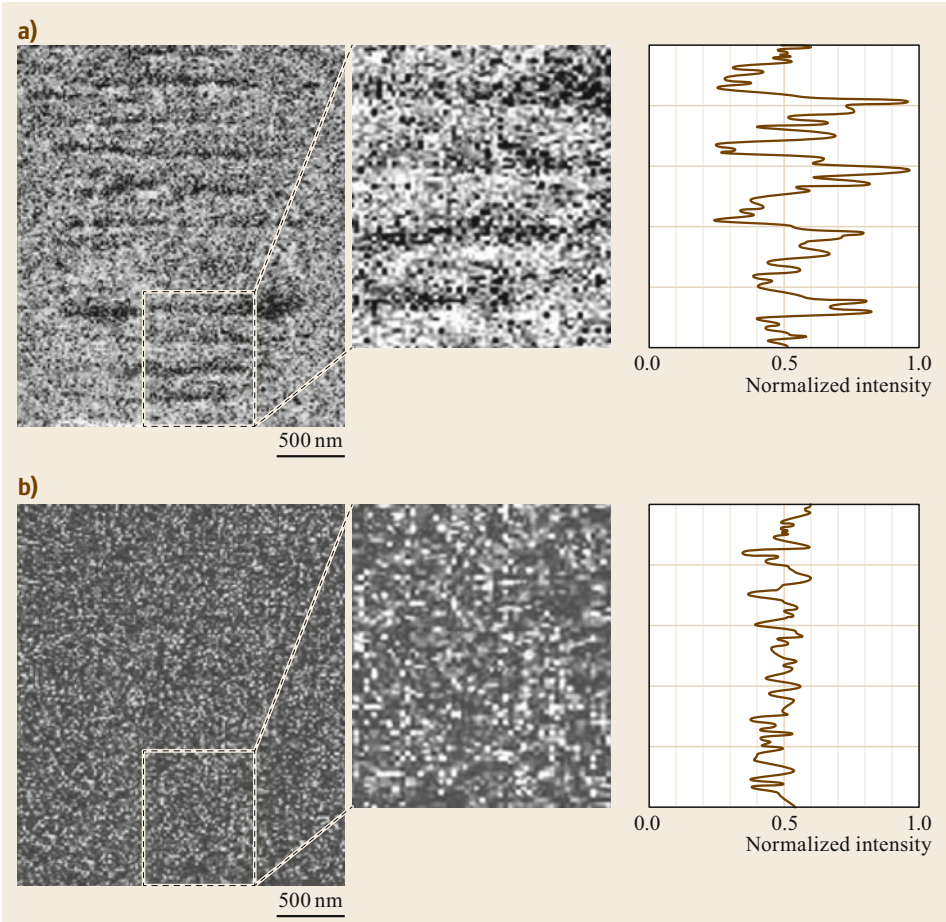

Fig. 11.25a,b Auger spectra maps and corresponding line profiles of **(a)** O and **(b)** Si on the same SiO_2 glass surface polished close to the depth of focal spot. Reprinted with permission from [11.96]. Copyright 2003 by the American Physical Society

GeO_2 glass. On the other hand, the BEIs clearly indicate that the stripe-like dark regions were periodically aligned perpendicular to the laser polarization direction. Previously, we have confirmed that such dark contrast in BEIs was caused by the periodic modulation of the oxygen defect concentration (Fig. 11.25).

In the case of SiO_2 glass, the fact that the Auger signal of oxygen in the dark contrast regions was low compared to other regions evidently indicates that the oxygen-deficient regions (SiO_{2-x}; $x \approx 0.4$) were periodically distributed. The diameters of the photoinduced structures for SiO_2 glass and GeO_2 glass were about 2.0 and 1.0 μm respectively (Fig. 11.19). We assumed that the difference in the size of the photoinduced regions, in which the polarization-dependent periodic nanostructures are formed, is derived from the self-focusing effect. Since the nonlinear self-focusing effect is initiated by the Kerr effect, the intensity-dependent refractive index is defined as [11.36]

$$n = n_0 + n_2 I \,, \tag{11.15}$$

where n_0 is the initial refractive index and I is the laser intensity. The nonlinear refractive index (n_2) in esu units is also given by [11.117]

$$n_2 = \frac{12\pi^2}{n_2^2 c}\chi^{(3)} \,, \tag{11.16}$$

where c is the speed of light and $\chi^{(3)}$ is the third-order nonlinear susceptibility. The beam waist diameter (w_0) is inversely proportional to the refractive index (n_0) and the nonlinear index change (Δn) under the self-focusing effect [11.118]

$$w_0 \propto \frac{1.22\lambda_0}{\sqrt{8n_0\Delta n}} \,, \tag{11.17}$$

where λ_0 is the laser wavelength. The laser pulse energy (E_p), w_0, n_0, and $\chi^{(3)}$ for SiO_2 glass and GeO_2 glass are listed in Table 11.4. The single bond strengths (B_{M-O}) for SiO_2 glass and GeO_2 glass are also shown [11.119].

Table 11.4 Typical femtosecond laser-irradiated condition, the minimum beam diameter w_0, the refractive index n_0, nonlinear susceptibility $\chi^{(3)}$, and single bond strength B_{M-O} from the literature for SiO_2 glass and GeO_2 glass

Material	E_p (μJ)	w_0 (μJ)	n_0	$\chi^{(3)}$	B_{M-O} (kJ/mol)	References
SiO_2 glass	1.0	≈ 2.0	1.45	2.8×10^{-14}	443	*Kim* et al. [11.120]
GeO_2 glass	0.2	≈ 1.0	1.61	4.5×10^{-13}	343	*Dimitrov* and *Sakka* [11.121]

At the present, mechanistic explanations of the polarization-dependent periodic nanostructure formation in glass have been proposed [11.96, 122–125]. The first model was proposed by an extension of the surface ripple formation theory and interpreted in terms of the interference between the incident light field and the bulk electron plasma longitudinal wave [11.96]. The initial model of photon–plasmon interference is proposed as follows. Since the incident photon energy ($\lambda = 800\,\text{nm} = 1.55\,\text{eV}$) is smaller than the energy gap of the material ($E_g = 9.1$ and $5.4\,\text{eV}$ for SiO_2 glass and GeO_2 glass respectively [11.121]), the ionization of the material at the focus of the intense femtosecond laser pulses takes place via multiphoton absorption. As a result, the multiphoton ionization under the sufficiently high light intensity (i. e., $\approx 10^{14}\,\text{W/cm}^2$) becomes dominant, followed by the formation of electron plasma [11.126]. The excited electrons oscillate in the electric field of the laser pulses, and then this oscillation is damped through electron–ion collisions [11.127]. The oscillatory energy of the excited electrons is converted into thermal energy by collisions with ions (inverse bremsstrahlung heating), and the temperature of the plasma also increases. The laser pulses can interact with the plasma only at frequencies $\omega_{ph} > \omega_p$, where ω_{ph} and ω_p are the light and plasma frequency respectively

$$\omega_p = \sqrt{\frac{e^2 N_e}{\epsilon_0 m_e}}\,, \tag{11.18}$$

where e is the electron charge, N_e is the electron density, and ϵ_0 is the permittivity of free space. The critical density N_{crit} ($\omega_p \approx \omega_p$) is

$$N_{crit} = \frac{\omega_{ph}^2 \epsilon_0 m_e}{e^2} = \frac{4\pi^2 \epsilon_0 m_e c^2}{e^2}\frac{1}{\lambda_0^2}\,, \tag{11.19}$$

which gives $N_{crit} = 1.7\times10^{21}\,\text{cm}^{-3}$ for $\lambda_0 = 800\,\text{nm}$. According to the theoretical calculation by the nonlinear optical Schrödinger equation with additional plasma generation terms, to reach the critical density, the absorption rate of laser energy about 10 times larger should be required [11.128]. The pump–probe experiments have also revealed that the permanent structural modification was observed at least at the electron density of $\approx 10^{19}\,\text{cm}^{-3}$ [11.129]. Furthermore, the 3-D finite-difference time-domain (FDTD) simulation results based on the Drude model have indicated that a plasma density of $5\times10^{20}\,\text{cm}^{-3}$ is most reproducible for the experimental observations [11.130]. Besides, the numerical simulations using the nonlinear Schrödinger equation show that an optical breakdown happens before the geometrical focus, leading to the formation of voids (type-III modification) under electron density of more than $10^{20}\,\text{cm}^{-3}$ [11.131]. Moreover, two-plasmon decay and stimulated Raman scattering instabilities can be observed in an underdense plasma at electron density ($N_e \approx N_{crit}/4$) [11.132]. Based on a mechanism analogous to the parametric decay of stimulated Raman scattering [11.133], assuming electrons with an electron temperature (T_e) of 10 eV are excited by the laser pulses with the intensity of $3\times10^{14}\,\text{W/cm}^2$, the threshold intensity for two-plasmon instability was estimated to be approximately $2.5\times10^{14}\,\text{W/cm}^2$. The intensity threshold (I_{th}) for two-plasmon decay instability is given by [11.134]

$$I_{th} = \frac{2.5\times10^{16} T_e}{\lambda L}\,. \tag{11.20}$$

Finally, the period (Λ) of the polarization-dependent nanostructure is obtained by following analytical expression

$$\Lambda = \frac{\lambda_0}{2c\sqrt{\frac{1}{3v_e^2\left(1-2\frac{\omega_p}{\omega_{ph}}\right)-\frac{N_e^2}{2c^2}\left(1-\frac{\omega_p}{\omega_{ph}}\right)}}}, \tag{11.21}$$

where v_e ($= 2\kappa_B T_e/m_e$) is the thermal speed of electrons and κ_B is the Boltzmann constant. This expression indicates that the period increases with increase of v_e and N_e. We believe that the generation of the $3/2\omega_{ph}$ harmonic observed in the experiments on femtosecond direct writing in SiO_2 glass is evidence for the two-plasmon decay [11.135, 136]. The other mechanism attempting to explain the polarization-dependent periodic nanostructure formation is the transient nanoplasmonic model [11.123, 124, 137]. This theory is the following: When the intense ultrashort light pulses are focused into transparent dielectrics, ionization hot spots can

be created in the vicinity of the focus, due to localized inhomogeneous nonlinear multiphoton ionization at generated defects or color centers. Hot spots produced in a previous laser pulse can evolve into spherical nanoplasmas [11.123, 124] during several subsequent pulses by a feedback mechanism based on the memory effect [11.138]. Due to such a memory effect, it is easier to ionize material on the next laser pulse. It should be noted that this effect does not cause any damage such as reduction of light transmission [11.138]. The initial underdense nanoplasmas ($N_e < N_{crit}$) grow gradually on successive pulses. The local field enhancement at the boundary of the nanoplasma promotes an asymmetric growth from the initial spherical plasma via ellipsoidal plasmas into plasma planes in the direction perpendicular to the laser polarization. The asymmetric growth of plasma accelerates as N_e approaches N_{crit}. The local electric fields at the equator ($E_{equator}$) and poles (E_{poles}) of the nanoplasma sphere for an overall electric field E will be the following

$$E_{equator} = \frac{3\epsilon_{dm}E}{\epsilon_{np} + 2\epsilon_{dm}} , \tag{11.22}$$

$$E_{poles} = \frac{3\epsilon_{np}E}{\epsilon_{np} + 2\epsilon_{dm}} , \tag{11.23}$$

where ϵ_{dm} and ϵ_{np} are the real parts of the permittivity for dielectric medium and nanoplasma respectively. The local field enhancement factor D_e is proportional to the ratio between the dielectric material and plasma permittivities [11.139]

$$D_e = \frac{E_{equator}}{E_{poles}} = \frac{\epsilon_{dm}}{\epsilon_{np}} . \tag{11.24}$$

For dielectric materials, the range of the subcritical plasma permittivity is confined to $0 < \epsilon_{np} < \epsilon_{dm}$. In these conditions ($D_e > 1$), the local field is enhanced towards the equator and suppressed at the poles. The plasma permittivity depends on the electron density

$$\epsilon_{np} = 1 - \frac{N_e}{N_{crit}} . \tag{11.25}$$

As N_e increases, the plasma permittivity decreases and reaches 0 at the plasma critical density. At these conditions, (11.24) predicts that very high enhancement factors are possible. The evolution of inhomogeneously localized nanoplasmas into plasma nanoplanes is shown schematically in Fig. 11.26. Multiple plasma nanoplanes in the focal volume are expected to affect the field propagation in a similar way to planar metallic waveguides, which leads to a prediction of nanostructure period equal to $\lambda/2n$.

11.3.4 Control of Self-Assembled Nanostructures (Type-II)

Up to now, several investigations regarding control of the period of the self-assembled nanostructure in silica glass by the laser parameters have been performed

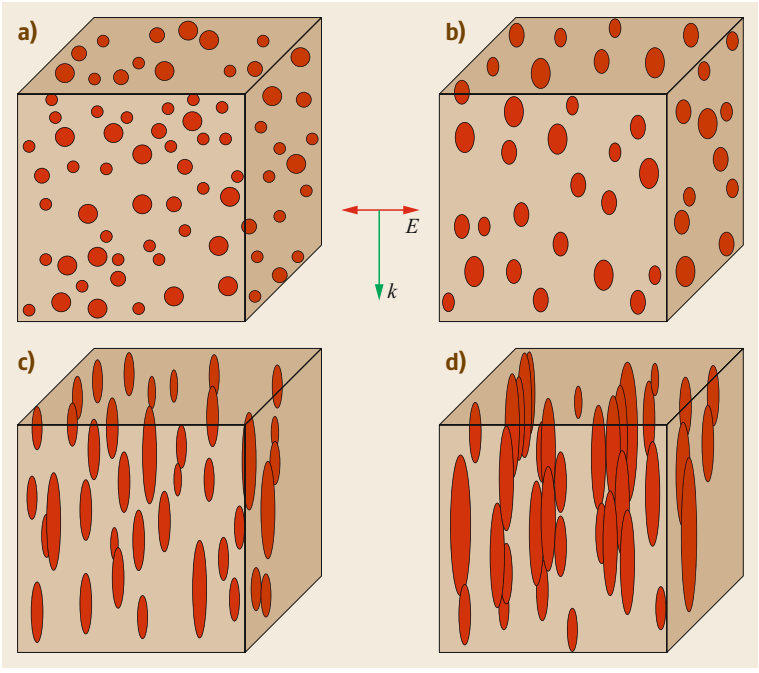

Fig. 11.26a–d Transient nanoplasmonic model based on the evolution of plasma nanospheres into nanoplanes. Randomly distributed plasma nanospheres (size is a few tens of nanometers) **(a)** grow asymmetrically in the presence of the laser field over hundreds of laser pulses (E and k indicate the polarization direction and laser propagation direction, respectively) **(b)** to become ellipsoidal **(c)** and finally flatten and merge to become micrometer-sized nanoplanes **(d)**. Reprinted with permission from [11.137]

[11.96, 100, 140, 141]. The grating periods against the laser wavelength, pulse energy, and number of pulses were linearly increased, decreased, and decreased, respectively. Recently, *Lancry* et al. have shown that such nanoplanes with oxygen defects are characterized by glass decomposition leading to nanovoid formation [11.142]. *Richter* et al. have also confirmed this nanoporosity using small-angle x-ray scattering [11.143]. The formation of these nanopores can be expected to enable new applications ranging from nanofluidics, chromatography and molecular sieves to five-dimensional (5-D) optical storage [11.101, 144, 145]. *Oliveira* et al. have also reported the formation of SiO_x nanocrystals within nanoplanes that is in agreement with oxide decomposition [11.146]. Although a significant birefringence in titanium silicate glass [11.147] and borosilicate crown glass [11.148] induced by femtosecond laser irradiation have been reported, no apparent birefringence has been observed in the case of BK7, Pyrex, soda-lime silicate glasses or $16SnO_2$-$84SiO_2$ [11.149]. In this section, polarization-dependent porous periodic nanostructures embedded in SiO_2 glass and GeO_2 glass are demonstrated. We also discuss the origin of the birefringence induced by creation of oxygen deficiencies and the nanopores [11.150]. To confirm the details of nanograting structures induced by femtosecond laser irradiation in SiO_2 glass and GeO_2 glass, we observed the cleaved surface along the nanoplanes with oxygen defects using a field emission scanning electron microscope (FE-SEM) [11.151]. It is possible to characterize the original cleaved surface without a conductive coating by applying a low accelerating voltage and very low current. Figure 11.27 shows SEIs on the cleaved surface of the writing regions in GeO_2 glass by femtosecond laser pulses with different pulse energy for each polarization. In the case of pulse energy of 0.2 μJ, these apparently show periodic nanostructures corresponding to areas of density contrast (Fig. 11.27a,b). Nanopores with diameters of approximately 10 nm were observed within the nanoplanes when the laser polarization was parallel to the writing direction (Fig. 11.27c,d). Evidently, these nanogratings consisting of mesoporous nanoplanes were self-aligned perpendicular to the laser

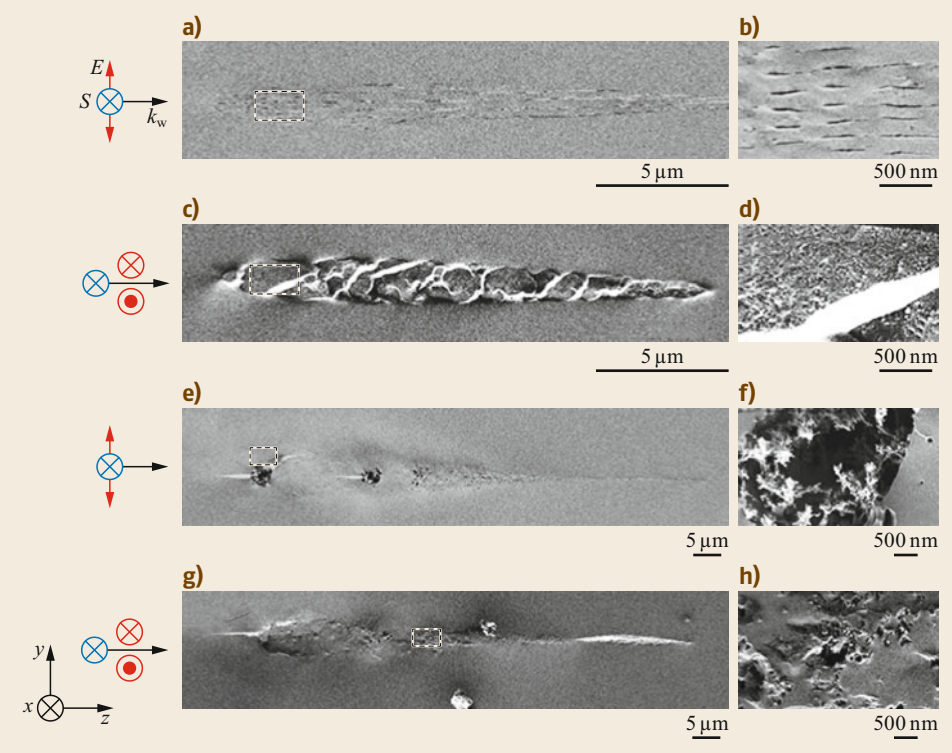

Fig. 11.27a–h SEIs of the cleaved surfaces including the laser traces written by femtosecond laser pulses with the E_p of **(a–d)** 0.2 μJ or **(e–h)** 2.4 μJ. The laser parameters were as follow: λ: 800 nm, τ_p: 70 fs, R_{rate}: 250 kHz, writing speed: 250 μm/s, objective: 0.80 NA. The polarization direction (E) was perpendicular **(a,b,e,f)** or parallel **(c,d,g,h)** to the writing direction (S). k_w indicates the laser propagation direction. High-magnification SEIs in the *dashed area* in **(a,c,e,g)** are also shown in **(b,d,f,h)**, respectively. Reprinted with permission from [11.150]

polarization. Such periodic nanostructures consisting of mesoporous nanoplanes cause the strong refractive index contrast, leading to the form birefringence. In the case of pulse energy of 2.4 μJ, hollow structures with multiple large voids of several micrometers were created (Fig. 11.27f,h). Based on the fact that the molecular O_2 was detected by Raman spectroscopy [11.142, 152], these voids are filled with O_2 generated by the decomposition of GeO_2 to $GeO_{2-x} + x/2O_2$. This phenomenon is similar to SiO_2 glass [11.96].

We compared the mesoporous nanoplanes for SiO_2 and GeO_2 glass (Fig. 11.28). Superficially regarded, the average size of nanopores in GeO_2 glass (< 10 nm) [11.150] was slightly smaller than that in SiO_2 glass (10∼30 nm) [11.142], though their packing density seems to be higher. The magnitude of birefringence can be expressed by the grating periodicity, the layer thickness, and the refractive indices of these two layers. The birefringence of the periodic nanostructure for ordinary (n_o) and extraordinary (n_e) waves is [11.115]

$$\Delta n = n_e - n_o = \sqrt{f n_1^2 + (1-f) n_2^2} - \frac{n_1 n_2}{\sqrt{f n_2^2 + (1-f) n_1^2}} , \quad (11.26)$$

where f is the filling factor, and n_1 and n_2 are the refractive indices for the platelets constituting the periodic nanostructure.

As shown in Fig. 11.29, these periodic nanostructures, in which thin regions of refractive index n_1 and larger regions of index n_2 are alternately formed, are aligned in the direction parallel to the laser polarization direction. In addition, based on the Maxwell–Garnett theory, the effective refractive index (n_1) of the mesoporous nanoplanes is [11.153]

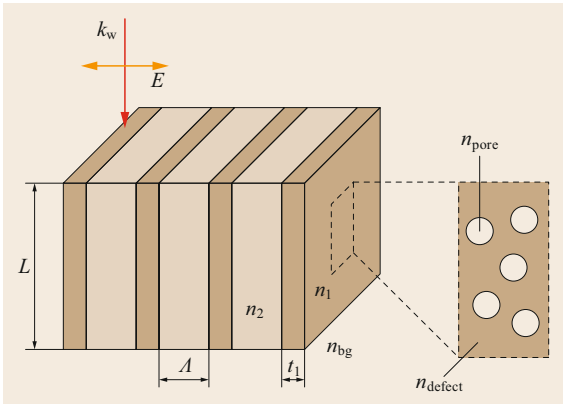

Fig. 11.29 Schematic of the nanograting structure photoinduced in the focal region. n_{bg}: refractive index of the initial glass, n_1, n_2: local refractive indices of nanoplane, $f = t_1/\Lambda$: filling factor, Λ: period of the nanograting, t_1: width of the region with index n_1, $n_{pore} = 1$: refractive index of the nanopore, n_{defect}: refractive index of the region surrounding the nanopores

$$n_1^2 = n_{defect}^2 \times \left[1 - \frac{3\phi(n_{defect}^2 - n_{pore}^2)}{2n_{defect}^2 + n_{pore}^2 + \phi(n_{defect}^2 - n_{pore}^2)}\right] , \quad (11.27)$$

where ϕ is the porosity, and n_{pore} (= 1) and n_{defect} are the refractive indices for the nanopores and for the surrounding oxygen defect regions, respectively.

We have evaluated the birefringence from the phase retardation measured by polarization microscopy ($\Gamma = LB$), where Γ is the measured phase retardation and B is the birefringence. The thickness (L) of the pho-

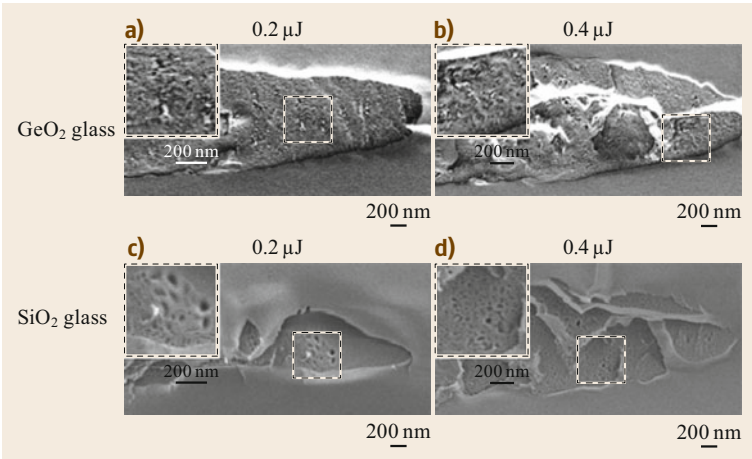

Fig. 11.28a–d SEIs of the cleaved surfaces including the laser traces in **(a,b)** GeO_2 glass and **(c,d)** SiO_2 glass written by femtosecond laser pulses with the E_p of **(a,c)** 0.2 μJ or **(b,d)** 0.4 μJ. *Insets* show the high-magnification SEIs in the *dashed areas*, respectively. Reprinted with permission from [11.150]

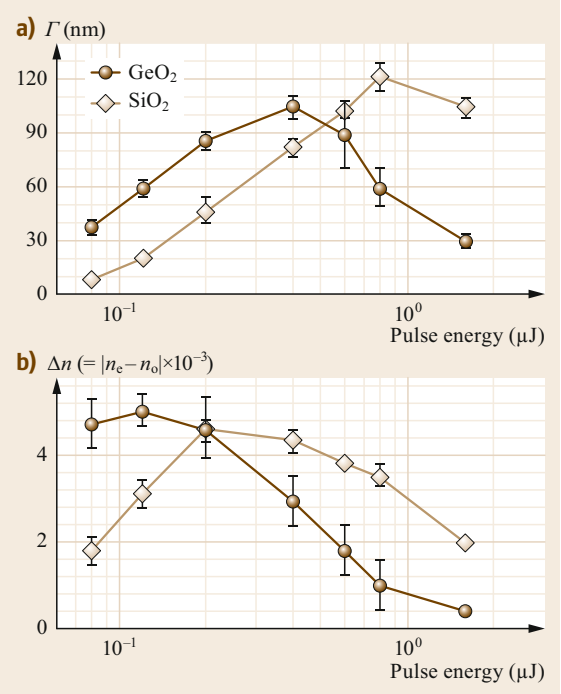

Fig. 11.30 **(a)** Phase retardation and **(b)** birefringence in GeO_2 and SiO_2 glass induced by femtosecond laser pulses as a function of the E_p. After [11.150]

toinduced periodic nanostructure along the laser propagation direction was determined by crossed-Nicols observation from the side of the sample. Initially, depending on the pulse energy, the Γ for both GeO_2 and SiO_2 glasses was increased, then decreased at 0.4 or 0.8 μJ, respectively (Fig. 11.30). On the other hand, the birefringence for GeO_2 glass was monotonically decreased, while in the case of SiO_2 glass, the birefringence was increased and then gradually changed to a decrease depending on the pulse energy. For SiO_2 glass, the maximum of birefringence was obtained at about 0.2 μJ. The higher birefringence for GeO_2 glass achieved by the lower pulse energy compared to SiO_2 glass is considered to be due to the ease of defect formation. Indeed, the birefringence of 0.005 for GeO_2 glass was obtained at a pulse energy of 0.12 μJ, compared to that of 0.003 for SiO_2 glass at the same pulse energy. Neglecting the effect on the refractive index change by the oxygen defects [11.154], our results are in good agreement with previous studies [11.98]. The parameters for calculation and the results are listed in Table 11.5.

It is known that GeO_2 glass is more thermodynamically unstable than SiO_2 glass, therefore two types of oxygen defects, such as the neutral oxygen monovacancy (NOMV; Ge–Ge) and the neutral oxygen divacancy (NODV; Ge^{2+}), are easily generated. Furthermore, it is also known that the structural relaxation of glass at about the glass transition temperature changes dramatically depending on impurities such as OH ions. We confirmed the decrease of birefringence associated with the annihilation of photoinduced defects by isochronal annealing experiments [11.150]. Figure 11.31 shows Arrhenius plots of the photoinduced phase retardation inside GeO_2 and SiO_2 glass by femtosecond laser pulses with a pulse energy of 0.2 and 0.4 μJ, respectively, as a function of the annealing temperature for 1 h. The amount of phase retardation after annealing at various temperatures are plotted against inverse temperature based on the Arrhenius equation

$$\frac{\Gamma_0 - \Gamma}{\Gamma_0} = A \exp\left(-\frac{E_a}{\kappa_B T}\right), \tag{11.28}$$

where Γ_0 and Γ are the phase retardation of the birefringent structure before and after successive annealing at various temperatures, respectively. Symbols of E_a, A, T, and κ_B are the activation energy for birefringence relaxation, the frequency factor, the absolute temperature, and the Boltzmann constant respectively. In the case of GeO_2 glass, the birefringent structures composed of the oxygen defects and nanopores were relaxed completely by annealing temperature, which is about 100 K higher than the glass transition point ($T_g \approx 823$ K). In good agreement with previously reported results [11.155, 156], the best linear fit was obtained with activation energy of 0.2 or 1.9 eV for GeO_2 or SiO_2, respectively. These results imply that the birefringence relaxation originates from oxygen vacancy annihilation.

Table 11.5 Parameters for calculation of local refractive index change in SiO_2 glass and GeO_2 glass

Parameters	SiO_2 glass	GeO_2 glass	Parameters	SiO_2 glass	GeO_2 glass
n_{bg}	1.454	1.645	n_{pore}	1	1
t_1^a	30 nm	50 nm	n_{defect}	1.454	1.645
Λ^b	200 nm	250 nm	ϕ	0.20	0.15
$f = t_1/\Lambda$	0.15	0.20	$n_1 - n_{bg}$	−0.092	−0.098
Δn	0.003	0.005	$n_2 - n_{bg}$	+0.035	+0.048

[a] The width of the region with index of n_1, [b] The period of nanogratings

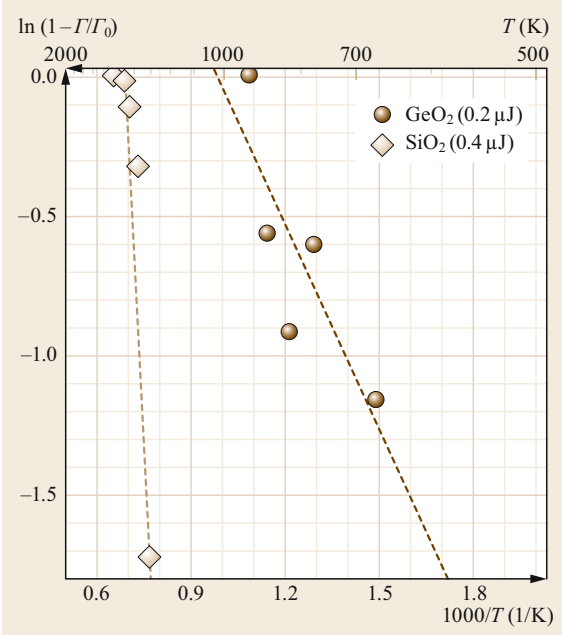

Fig. 11.31 Arrhenius plots of photoinduced phase retardation in GeO_2 and SiO_2 glass by femtosecond laser pulses as a function of the annealing temperature for 1 h. The E_p for GeO_2 and SiO_2 glass was 0.2 and 0.4 μJ, respectively. After [11.150]

Table 11.6 Anion concentration in SiO_2 glass samples

Sample	OH (ppm)	Cl (ppm)	F (ppm)	Refractive index
HO100	100	0.1	< 1	1.457
HO500	500	< 1	< 1	1.457
HO1000	1000	100	< 1	1.457
CL6300	< 1	6300	< 1	1.458
F9400	< 1	< 1	9400	1.453

We have also confirmed the effect of the impurities in SiO_2 glass on the annihilation of photoinduced Γ by thermal treatment [11.157]. In these experiments, we used SiO_2 glass samples doped with anions of Cl, F, and OH (Table 11.6). After birefringent structure formation by femtosecond laser irradiation inside various anion-doped SiO_2 glasses, we observed annihilation of the photoinduced Γ under annealing at various temperatures (Fig. 11.32). The temperature at the steep decrease of the Γ was affected by the doped anion species in glass, which were approximately their T_g (Fig. 11.32a). The differences in the temperature at the relaxation of birefringent structure, including the oxygen defects and nanopores, were considered to be caused by the difference in the amount of oxygen deficiency defects brought by the doped anion species in glass. Although the size of nanopores and the porosity in the nanoplanes with oxygen defects did not change below the glass transition temperature, we assumed that nanopores in glass start to be eliminated at about the glass transition temperature, where the Γ began to decrease steeply [11.157]. We have also confirmed that the thermal stabilities became higher in various anion-doped SiO_2 glass in the order OH100 > Cl6300 ≃ OH1000 > F9400 (Fig. 11.32b). From these results, we can conclude that the doped anion species and their concentrations are dominant factors in the formation of the photoinduced birefringent structure.

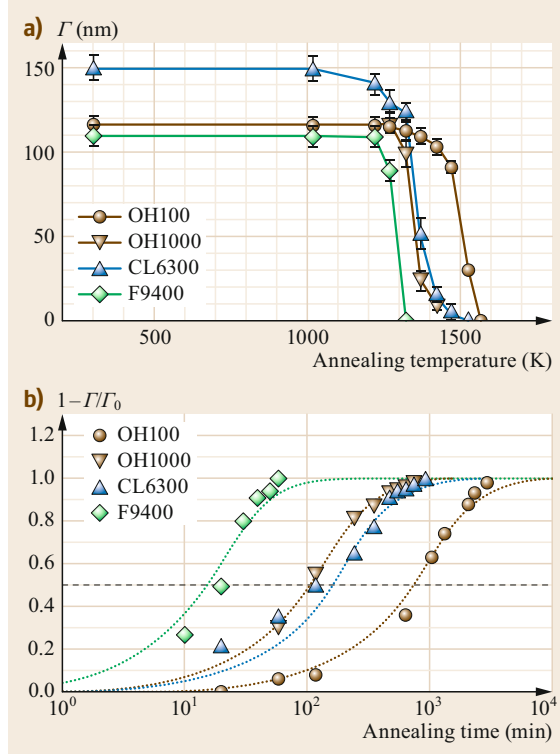

Fig. 11.32 **(a)** Phase retardation (Γ) of birefringence exhibited by the nanogratings after annealing at various temperatures for 1 h. **(b)** Plots of the change ratio of the photoinduced Γ in SiO_2 glass samples including various anion dopants. *Dotted lines* show fitting curves with $y = 1 - \exp(-ax)$. *Dashed line* shows the half value of the initial phase retardation (Γ_0). After [11.150]

11.3.5 Evolution of Optical Anisotropy

To expand the application of polarization-dependent photosensitivity in glass, we focus on the controllability of birefringence induced by femtosecond double pulses using three different experimental configurations. First, to reveal the effect of the temporally shaped femtosecond laser pulses, the double pulses

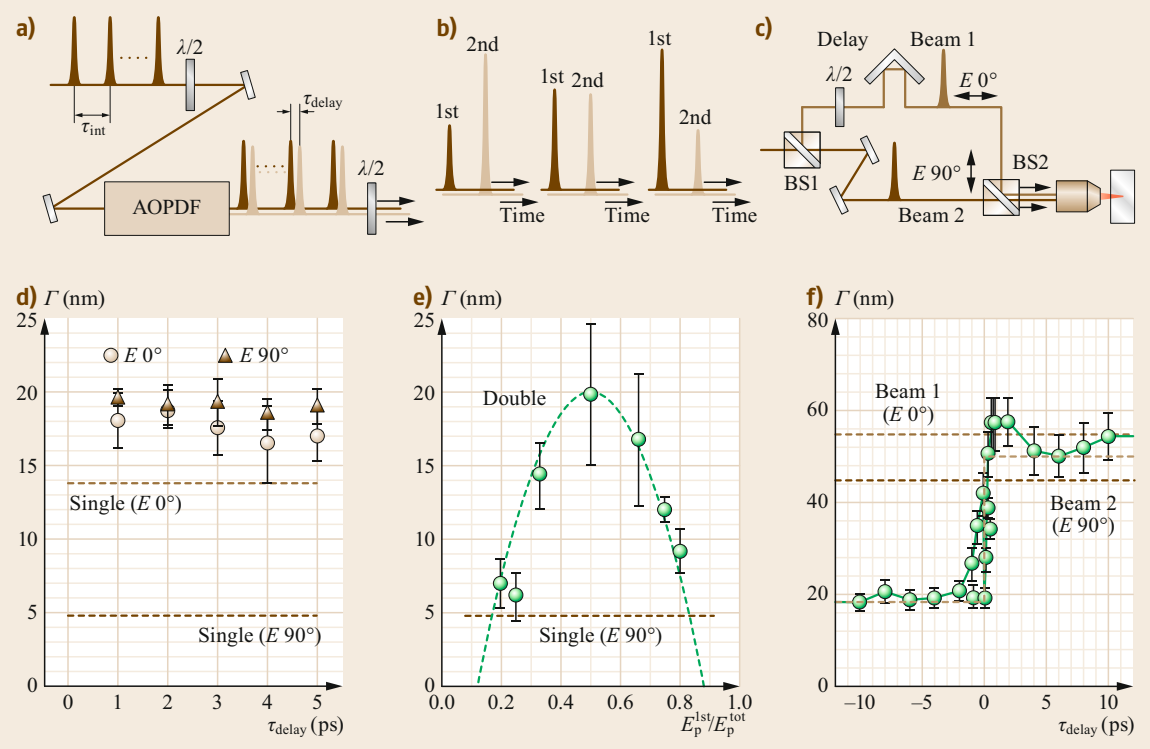

Fig. 11.33a–f Schematic of three different experimental configurations: **(a)** time-delayed double pulses with the same linear polarization direction, **(b)** time-delayed double pulses with various intensity ratios (polarization direction: E 90°), and **(c)** time-delayed double pulses in mutually orthogonal polarization directions. AOPDF: acoustic optic phase dispersion filter, $\lambda/2$: half-wave plate, BS1, BS2: polarizing beam splitters, delay: optical delay line. **(d)** Plots of the phase retardation (Γ) versus τ_{delay} induced by the linearly polarized double pulses (*light brown*: E 0°, *dark brown* E 90°). The Γ values for single pulses ($E_p = 0.68\,\mu J, N_{pulse} = 100$) with each polarization direction are also shown. **(e)** Plots of the Γ versus E_p^{1st}/E_p^{tot} induced by the linearly polarized double pulses (E 90°, $\tau_{delay} = 3$ ps, $E_p = 0.68\,\mu J$). *Dashed green line* in **(e)** indicates the quadratic fitting for eye guidance. **(f)** Plots of the Γ versus delay induced by the orthogonally polarized double pulses ($E_p = 1.0\,\mu J$, $N_{pulse} = 250\,000$). The Γ values for single pulses with each polarization direction are also shown. *Beige dotted line* in **(f)** indicates the fitting curve by Gaussian integral function

in parallel polarization direction with each other with the time delay (τ_{delay}) up to 5 ps were produced using an acousto-optic phase dispersion filter (AOPDF) (Fig. 11.33a). The total pulse energy and the irradiated number of pulses (N_{pulse}) were fixed at 100 shots and 0.68 μJ, respectively. In the second experiments, the pulse energy ratios of the first pulses (E_p^{1st}) to the total pulse energy ($E_p^{tot} = E_p^{1st} + E_p^{2nd} = 0.68\,\mu J$) were changed (Fig. 11.33b). The polarization direction, τ_{delay} and the N_{pulse} were set to be vertical (E 90°), 3 ps and 100 shots, respectively. The double pulses with various τ_{delay} and E_p^{1st}/E_p^{tot} were produced by changing the second-order dispersion component of pulse shape. The interpulse time (τ_{int}) was fixed at 0.1 ms. We also performed the experiments using double pulses with various τ_{delay} and the mutually orthogonal polarization direction on each other (Fig. 11.33c). The detailed optical system has been reported elsewhere [11.101]. The E_p of orthogonally polarized double pulses and the N_{pulse} were fixed at 1.0 μJ (= 0.5 μJ + 0.5 μJ) and 250 000 shots, respectively. In the all experiments, the laser power was independent of the polarization direction. The photoinduced birefringent structures were inspected by a polarization microscope to measure the phase retardation (Γ). From the results of the first experiments (Fig. 11.33d), interestingly, the Γ induced by the single pulses with horizontal (E 0°) or vertical (E 90°) polarization direction was apparently different regardless of the same pulse energy. Meanwhile, there was no big difference in the Γ in the case of the double pulses [11.144]. Furthermore, the Γ induced by the double pulses was larger than that for single pulses

in τ_{delay} up to 5 ps. This phenomenon is interpreted in terms of the enhancement of electron excitation via the laser-plasma interaction during the lifetime of plasma excited by the first pulses [11.158]. From the results of the second experiments (Fig. 11.33e), the Γ reached a maximum at the one-to-one double pulses. In addition, the Γ was symmetrically changed with respect to the equally divided double pulses. The enhancement effect on the generation of free electrons excited by the first pulses was remarkable for the E_p^{1st}/E_p^{tot} ranging from 0.2 to 0.8. The origin of the symmetric variation of the Γ to the E_p^{1st}/E_p^{tot} is considered to be as follows. The electron-hole pairs are produced through multiphoton absorption by the first pulses. The excited electrons absorb even more laser energy leading to the increase of electron temperature and density (avalanche ionization). Such an electron plasma is relaxed first by electron–phonon coupling, then via radiative and/or nonradiative transition, and eventually an oxygen-deficient center is formed. If the second pulses arrive before the lifetime of electron plasma, the second pulses are employed to assist the avalanche ionization [11.159]. Assuming that the ionization processes for the first pulses and the second pulses are independent from each other as multiphoton ionization and avalanche ionization, respectively, in a series flows of the electron excitation by double pulses, the Γ to the E_p^{1st}/E_p^{tot} could change symmetrically. On the other hand, the asymmetric evolution of Γ was also unambiguously induced by the orthogonally polarized double pulses on each other, regardless of the fact that the pulse energy and pulse duration were set at the same conditions (Fig. 11.33f). In the case of single pulses, a small difference in the Γ existed depending on the polarization direction; however, the difference for the orthogonally polarized double pulses was several times larger. Such asymmetric change of Γ for orthogonally polarized double pulses could be interpreted as follows. Assuming that horizontal and vertical polarized pulses produce different heating, and vertical pulses produce more heating than horizontal pulses, the horizontally polarized first pulses in the next double pulses may not completely erase the birefringent structure produced by the vertically polarized second pulses in the previous double pulses. In contrast, when the pulse sequence is reversed, the vertically polarized first pulses in the next double pulses will erase the birefringent structure produced by the horizontally polarized second pulses in the previous double pulses. Finally, such asymmetric photosensitivity of glass induced by the orthogonally polarized double pulses is considered to be derived from femtosecond pulses with tilted intensity fronts exhibiting a nonreciprocal quill writing effect [11.101, 160].

We have also inferred the formation dynamics of the periodic nanostructure based on the Γ change induced by the double pulses with longer delays up to 1700 ps. In these experiments, the E_p^{tot} and the N_{pulse}

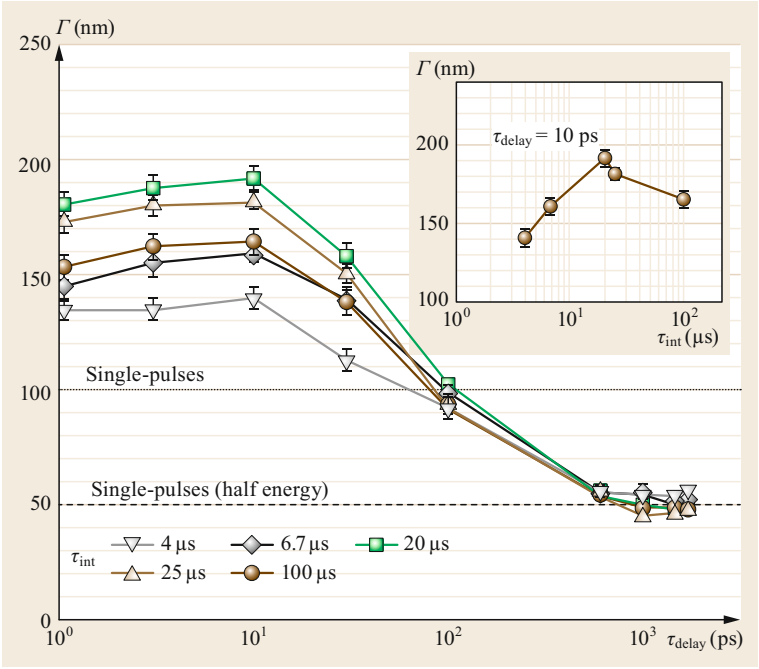

Fig. 11.34 Variation of the Γ as a function of the τ_{delay} for each τ_{int}. *Inset* shows the Γ versus τ_{int} at $\tau_{delay} = 10$ ps. *Dashed* and *dotted lines* are the Γ values induced by the single pulses with the same or half energy, respectively

were fixed at 0.5 μJ and 100 shots respectively. Figure 11.34 shows the variation of the Γ as a function of the τ_{delay} for each τ_{int}. As the reference, the single-pulse experiments with the same or the half E_p were also performed. The Γ initially slightly increased and then reached the maximum at about 10 ps. Despite the same E_p^{tot}, the Γ for double pulses were up to twice as large as those for single pulses. Thereafter, the Γ asymptotically approached the Γ induced by the single pulses with the half-pulse energy ($E_p = 0.25$ μJ). The decrease of Γ suggests that the free electrons excited by the first-arrival pulse in double pulses have been relaxed before the arrival of the delayed second pulse. Furthermore, the asymptotic behavior could be interpreted in terms of the memory effect arising from metastable color centers or permanent changes in electronic structure associated with chemical reorganization [11.123]. The Γ also depended on the pulse repetition rate, i. e., interpulse time (τ_{int}). The optimal τ_{int} to obtain the maximum Γ was 20 μs corresponding to R_{rate} of 50 kHz [11.161]. As mentioned in the previous section, since the excessive thermal accumulation occurred when $\tau_{int} < 20$ μs, we speculate that the structural relaxation of oxygen defects and/or nanopores temporarily formed makes the Γ value smaller [11.101]. On the other hand, the reason for the smaller Γ for $\tau_{int} > 20$ μs is considered to be caused by the decrease in nonlinear absorptivity depending on the thermally excited electrons.

Considering the energy levels of SiO_2 glass excited by femtosecond double pulses (Fig. 11.35), the maximum Γ value obtained at 10 ps suggests that this timescale is similar to the nonradiative relaxation lifetime from the self-trapped excitons (STEs) [11.162]. Since the electrons once excited by the first-arrival pulse are trapped at STEs, it becomes easy to interact with the second-arrival pulse. Finally, the enhancement effect of the interaction between the electrons trapped at STE level and the second-arrival pulse continues during several hundred picoseconds, which corresponds to the STE decay time.

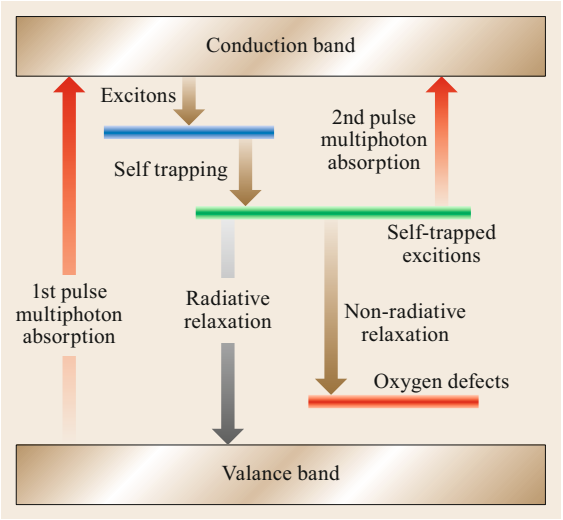

Fig. 11.35 Schematic of the dynamics model of oxygen defect generation in SiO_2 glass

11.4 Anisotropic Photosensitivity of Glass

As mentioned in the above sections, photosensitivity, the term given to describe an object's response to light, is a material property that is relevant to many phenomena and applications ranging from photosynthesis, photography and optical data storage to ultrafast laser writing. It has been a common belief that, in the case of an isotropic medium such as glass, if you change the polarization of an isotropic laser beam, the photosensitivity and the corresponding photoinduced material modifications would not change. However, a single intense ultrashort pulse laser beam with a tilted pulse front can interact with the glass differently depending on the light polarization. Typically, optical anisotropy manifests itself as differing responses of the material to light with different polarizations [11.163]. Optical anisotropy may have a microscopic origin being attributed to material structure (e. g., crystal [11.164]). In addition, the external stress or polarized light (photoinduced birefringence) can also produce such a phenomenon [11.165]. Furthermore, optical anisotropic phenomena may originate from gradients, or macro- or subwavelength scale interfaces (form birefringence) [11.115]. Apparently, in an isotropic medium including a glass, the optical anisotropy is forbidden by symmetry, i. e., such a medium responds equally to light with different polarizations. Therefore, photosensitivity of glass, including nonlinear optical phenomena such as multiphoton absorption and optical Kerr effect, is not affected by the light polarization direction. Recently, two remarkable phenomena relating to nonreciprocal photosensitivity induced by femtosecond laser pulses have been reported. The first is a nonreciprocal response that is a material modification depending on light propagation direction in a noncentrosymmetric crystal [11.166]. The second is a quill writing effect that is a material modification depending on the laser writing di-

rection in glass [11.160, 167, 168]. Such nonreciprocal photosensitivities are considered to relate to the mutual orientation of the light polarization azimuth and the pulse front tilt (PFT) [11.169]. The PFT is a tilt between the pulse front and a direction perpendicular to the beam, which is particularly notable for broadband pulses such as femtosecond laser pulses. Femtosecond laser pulses with different polarization directions were focused in a dot shape inside aluminosilicate glass via 50×, NA 0.80 objective. The glass composition was $67.8SiO_2$-$17CaO$-$10.6Al_2O_3$-$4.6B_2O_3$ (mol%). The laser parameters were as follows: λ: 800 nm, τ_p: 70 fs, R_{rate}: 250 kHz, E_p: 2.4 μJ. To reveal the effect of the PFT on the photoinduced structure in glass, the beam shape and the power were set as the same after passing through the microscope objective for all polarization directions. Although there was no apparent asymmetry in the laser intensity distribution in focal plane, unexpectedly, the intensity of the white light emission from the focal region depended clearly on the polarization direction (Fig. 11.36a). Furthermore, despite the time-integrated intensities of white light being almost the same, the temporal light intensity at 615 nm during laser irradiation was apparently different according to the laser polarizations (Fig. 11.36b).

The photoinduced structures were also different according to the polarization directions. In particular, at a certain polarization, strong coloration regions surrounded by asymmetrically distributed bubbles were observed (Fig. 11.37a,b). Such colored regions correspond to the element migration region caused by the high fluence and heat accumulation [11.35, 41, 45]. The Raman spectra of the photoinduced structures were also different according to the polarization directions (Fig. 11.37c,d). Line profiles along the photoinduced structures clearly indicated the difference in the peak intensities at about 150∼190 and 500 cm^{-1}. These are assigned to the coupled tetrahedral SiO_4 groups [11.170, 171] and the bending vibration modes of Si(Al)−O−Si(Al) bridges in glass [11.172], respectively.

We have also observed light absorption at the coloration region, indicating that the absorbance was changed in a cosine-like dependence on the polarization azimuth angle α (Fig. 11.38a). The refractive index changes were also observed by using a quantitative phase imaging (Fig. 11.38b). The refractive index change (Δn) is estimated from

$$\Delta n = \frac{\Delta\varphi\lambda}{2\pi d}\,, \tag{11.29}$$

where $\Delta\varphi$ is the phase shift at wavelength λ and d is the thickness of the structure along the light propagation direction. The map of the phase shift at $\lambda = 550$ nm corresponding to the refractive index change is also shown in Fig. 11.38c. Assuming $d \approx 20\,\mu$m, the minimum value of about $\Delta n \approx -2\times10^{-2}$ was obtained at the polarization azimuth $\alpha = 90$ and 270°. From these results, since all the laser parameters except polarization direction were set the same, the photosensitivities of glasses induced by femtosecond laser pulses are clearly anisotropic according to the laser polarization direction.

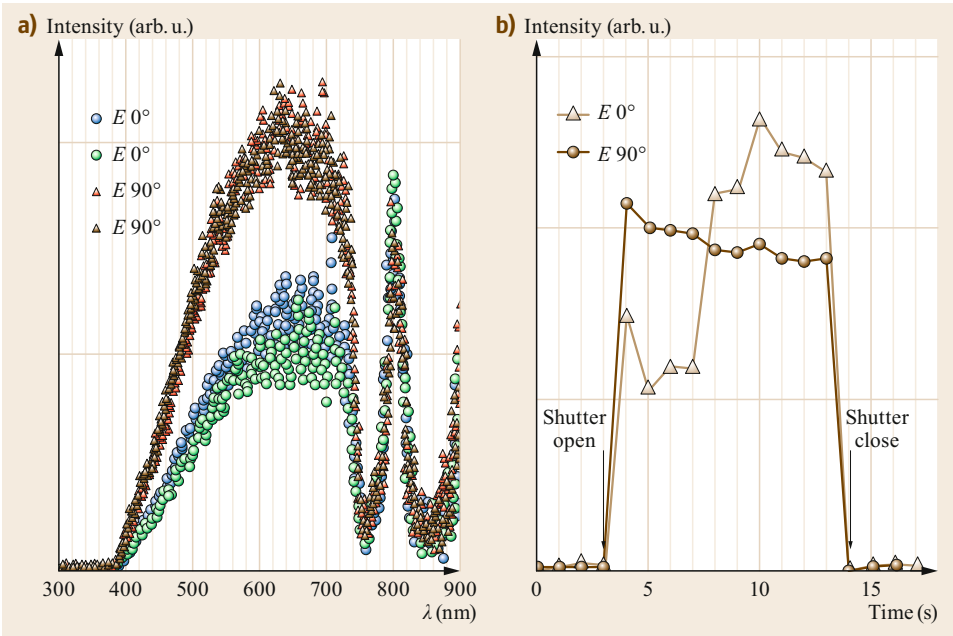

Fig. 11.36 (a) Emission spectra from focus in SiO_2 glass during exposure of femtosecond laser pulses with mutually orthogonal polarization directions. The pump laser power at 800 nm was reduced by a factor of 10^5 using a notch filter. The results of two independent measurements for each polarization show good reproducibility. (b) Temporal changes of light intensity at 615 nm as a function of irradiation time

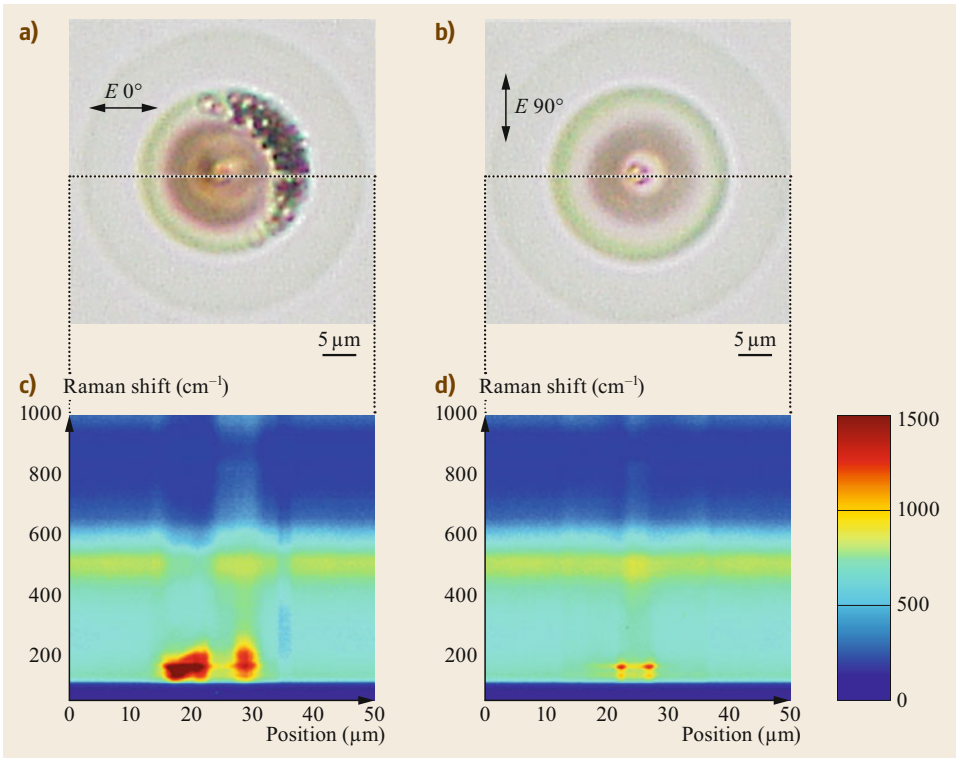

Fig. 11.37 (a,b) Optical microscope images of the modified regions by the femtosecond laser pulses with mutually orthogonal polarization directions. (c,d) Profiles of Raman spectra along the *dotted lines* in (a,b). From [11.169]

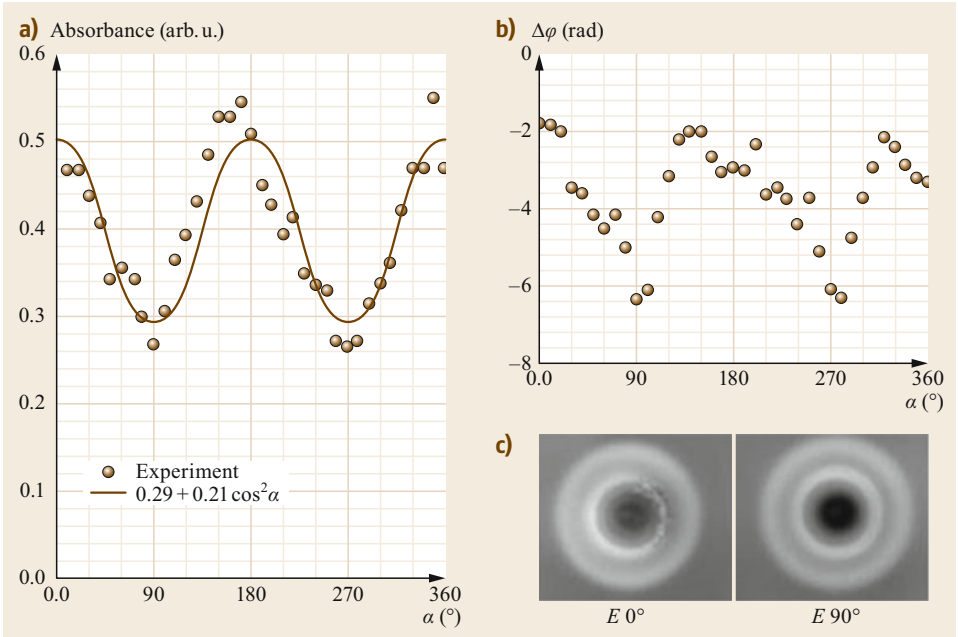

Fig. 11.38 (a) Absorbance of the modified region for 400 nm as a function of the polarization angle (α) of writing femtosecond laser pulses. *Line* indicates the fitting curve by $\cos 2\alpha$. (b) Photoinduced phase change in the center of a modified region as a function of α. (c) Maps of phase change for the modified regions by femtosecond laser pulses with mutually orthogonal polarization directions. *Darker contrast* corresponds to more negative index change. From [11.169]

By using the GRENOUILLE device, we have characterized the spatiotemporal properties of our femtosecond laser pulses (Fig. 11.39). This indicated that our laser pulses have Gaussian intensity profiles and a small PFT of about 1.8 fs/mm. We believe that such a small PFT was derived from a slight misalignment of the prism pair or a slight beam divergence [11.173, 174]. Since the PFT is proportional to the beam diameter and can be significantly increased in the vicinity of the beam waist, we estimated that PFT reaches ≈ 180 fs/mm 10 μm before the geometrical focus in air.

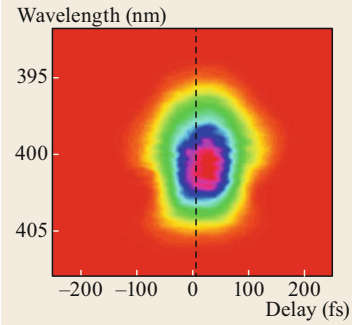

Fig. 11.39 Typical measured GRENOUILLE trace. The *black dashed line* indicates zero delay. The shift of the trace center in delay axis indicates the PFT. From [11.169]

11.5 Nonreciprocal Photosensitivity of Glass

The control of the quill writing effect caused by the anisotropic trapping of the electron plasma by the PFT enables the formation of the individual photoinduced structures, i. e., type-II or type-II modifications in silica glass [11.160]. To visualize the effect of the PFT, we have observed the photoinduced structure by switching the sign of the PFT [11.167]. The four laser-written traces with alternating writing directions were induced by scanning the focus spot with pulse energy of 1.4 μJ and writing speed of 50 μm/s (Fig. 11.40). The laser-written traces clearly indicate the directional dependence (i. e., traces in right-to-left: type-II modification, traces in left-to-right: type-III modification) (Fig. 11.40a). By adding a mirror in the experimental configuration, we reversed the direction of the PFT (Fig. 11.40b). The directional dependence was clearly changed in reverse. Comparing these results, the photoinduced structures written by the opposite direction of the PFT provide evidence that the PFT is responsible for the directional dependence in the photosensitivity induced by the femtosecond laser.

Such directional dependence of structural modification provided by the direction of the PFT is also related to the previously mentioned polarization-dependent heating phenomenon. We have also observed weak dependence of the absorbed laser power, and in contrast, strong dependence of the hot plasma emission on the polarization direction. From these results, we specu-

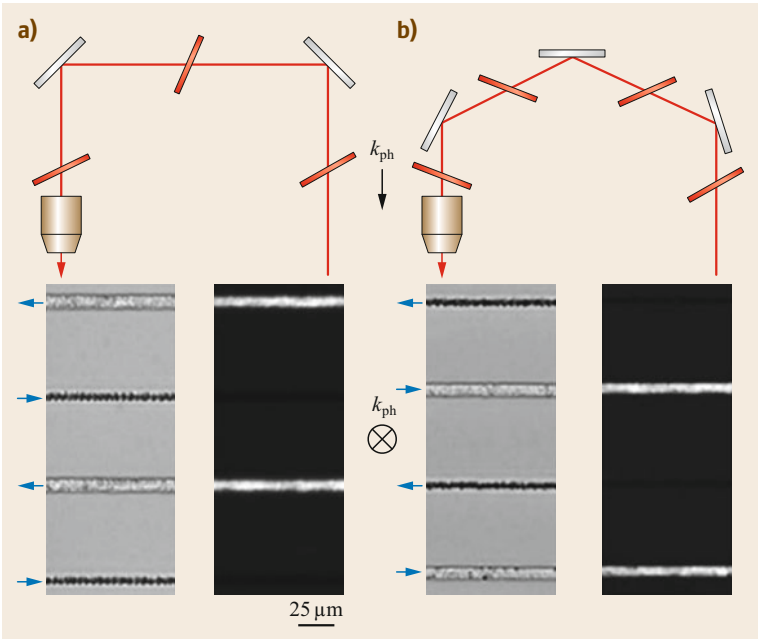

Fig. 11.40a,b Microscope images inspected without polarizers (*bright images*) and with crossed polarizers (*dark images*) of the laser traces written by femtosecond laser pulses. To switch the sign of the PFT, experimental configurations with **(a)** two mirrors or **(b)** three mirrors were employed. *Red lines* show the PFT. k_{ph} is the laser propagation direction. Reproduced from [11.167], with the permission of AIP Publishing

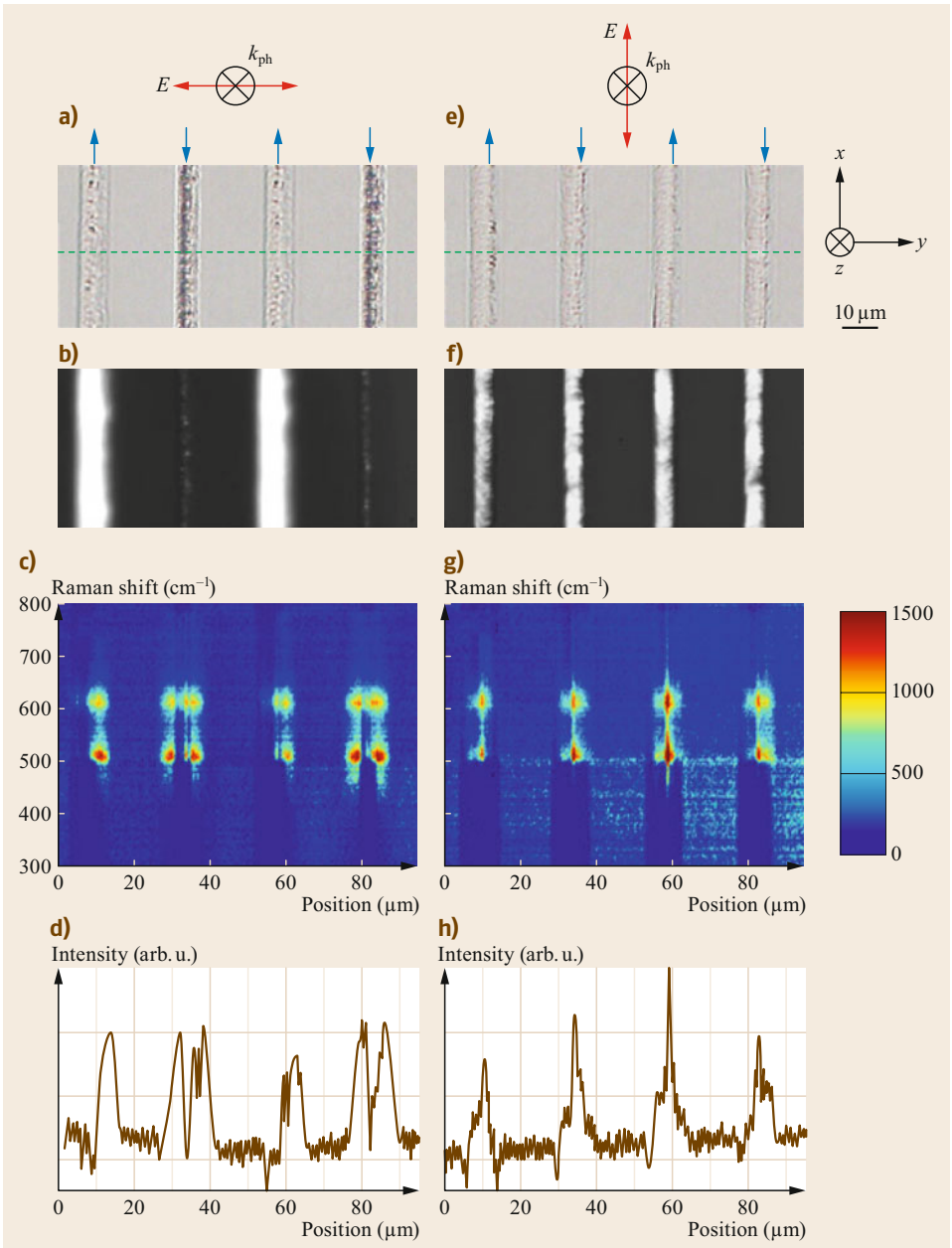

Fig. 11.41a–h
Nonreciprocal structural changes in silica glass. The *top schematics* indicate the direction of laser polarization (E) and propagation (k_{ph}). Images in Nomarski-DIC **(a,e)** and crossed-polarizers **(b,f)** of the lines written with orthogonally polarized femtosecond laser pulses. *Blue arrows* show the writing directions. The laser parameters were as follows: λ: 800 nm, τ_p: 70 fs, R_{rate}: 250 kHz, E_p: 2.0 J, writing speed: 100 µm/s, objective: 0.80 NA. **(c,g)** Profiles of Raman spectra along the *green dotted lines* in **(a,e)**. Raman intensity profiles at 492 cm^{-1} (D1) are also shown in **(d,h)**

lated that two different types of excitation are photoinduced, despite the absorbed laser energy not changing in the polarization direction. One is an isotropic heating by electron acceleration via inverse bremsstrahlung and the other is an anisotropic strong heating provided by the mutual direction of the polarization and the PFT [11.169]. Such nonreciprocal photosensitivity of glass induced by the femtosecond laser with suitable PFT can effect the structural change in glass (Fig. 11.41a,b,e,f). A series of laser traces were photoinduced in silica glass by alternately switching the writing direction. Similar to the previously mentioned experiments in Fig. 11.37, all the laser parameters except the polarization direction were set the same. The pulse energy and the writing speed were 2.0 µJ and 100 µm/s respectively. The laser-written traces were observed by optical microscope under a Nomarski-DIC illumination (back-illumination) or a crossed-polarized (CP) configuration. These images indicate that the nonreciprocal photosensitivity appearing as the difference

in the structural modification is tunable by the polarization direction. Indeed, the structural densification was also effected by the nonreciprocal photosensitivity (Fig. 11.41c,d,g,h). For a certain polarization direction to the laser writing direction, the intensity distribution of the characteristic Raman peak at $492\,\mathrm{cm}^{-1}$ (D1), suggesting structural densification, became asymmetric. Detailed analysis of these Raman shifts towards higher frequency revealed that a large stress of about 3.2 GPa was applied in the birefringent structures. This is in good agreement with the calculation from the phase retardation ($\Gamma = \gamma dP$), where γ is the photoelastic constant of silica glass ($\approx 3.5\,\mathrm{nm/(cm\,MPa)}$), P is the internal stress, and $d = 4\,\mu\mathrm{m}$ is the length of the photoinduced structure. On the other hand, the structural densification was observed at the edge of the collateral damage. We attribute this new type of light-matter interaction to the spatiotemporal couplings in ultrashort light pulses. We anticipate that the nonreciprocal photosensitivity of glass induced by ultrashort laser pulses will open the door for a novel light-matter interaction.

References

11.1 D. Dolbashian: Pliny the Elder (Gaius Plinius Secundus), Historia Naturalis, about AD 77, http://www.cmog.org/article/pliny-elder-gaius-plinius-secundus-historia-naturalis-about-ad-77

11.2 W.W. Shaver: Recent developments in glass research. In: *Symp. Mater. Res. Front., Boston* (ASTM, West Conshohocken 1959) pp. 43–48

11.3 S.D. Stookey: Photosensitive glass, Ind. Eng. Chem. **41**, 856–861 (1949)

11.4 W.H. Armistead: Silver-containing photosensitive glass, Canadian Patent No. 442272 (1947)

11.5 E.D. Zanotto: Metastable phases in lithium disilicate glasses, J. Non-Cryst. Solids **219**, 42–48 (1997)

11.6 N.F. Borrelli, B. Wedding: Optical properties of chemically reduced photochromic glasses, J. Appl. Phys. **63**, 2756–2759 (1988)

11.7 N.F. Borrolli, J.B. Chodak, D.A. Nolan, T.P. Seward: Interpretation of induced color in polychromatic glasses, J. Opt. Soc. Am. **69**, 1514–1519 (1979)

11.8 Y. Paz, Z. Luo, L. Rabenberg, A. Heller: Photooxidative self-cleaning transparent titanium dioxide films on glass, J. Mater. Res. **10**, 2842–2848 (1995)

11.9 K.O. Hill, Y. Fujii, D.C. Johnson, B.S. Kawasaki: Photosensitivity in optical fiber waveguides: Application to reflection filter fabrication, Appl. Phys. Lett. **32**, 647–649 (1978)

11.10 H. Hosono, Y. Abe, D.L. Kinser, R.A. Weeks, K. Muta, H. Kawazoe: Nature and origin of the 5-eV band in SiO_2:GeO_2 glasses, Phys. Rev. B **46**, 11445–11451 (1992)

11.11 P. Cordier, J.C. Doukhan, E. Fertein, P. Bernage, P. Niay, J.F. Bayon, T. Georges: TEM characterization of structural changes in glass associated to Bragg grating inscription in a germanosilicate optical fibre preform, Opt. Commun. **111**, 269–275 (1994)

11.12 H. Hosono, J. Nishii: High photosensitivity and nanometer-scale phase separation in GeO_2–SiO_2 glass thin films, Opt. Lett. **24**, 1352–1354 (1999)

11.13 J. Nishii, K. Kintaka, H. Nishiyama, M. Takahashi: Photosensitive and a thermal glasses for optical channel waveguides, J. Non-Cryst. Solids **326/327**, 464–471 (2003)

11.14 A. Sakoh, M. Takahashi, T. Yoko, J. Nishii, H. Nishiyama, I. Miyamoto: Photochemical process of divalent germanium responsible for photorefractive index change in GeO_2–SiO_2 glasses, Opt. Express **11**, 2679–2688 (2003)

11.15 R.M. MacFarlane, R.M. Shelby: Homogeneous line broadening of optical transitions of ions and molecules in glasses, J. Lumin. **36**, 179–207 (1987)

11.16 K. Hirao, S. Todoroki, K. Tanaka, N. Soga, T. Izumitani, A. Kurita, T. Kushida: High temperature persistent spectral hole burning of Sm^{2+} in fluorohafnate glasses, J. Non-Cryst. Solids **152**, 267–269 (1993)

11.17 A. Kurita, M. Tanaka, T. Hiyama, A. Hada, T. Kushida: Wavelength dependence of persistent spectral hole burning in Sm^{2+}-doped fluoride glasses, J. Luminescence **64**, 167–171 (1995)

11.18 K. Fujita, K. Tanaka, K. Hirao, N. Soga: Room-temperature persistent spectral hole burning of Eu^{3+} in sodium aluminosilicate glasses, Opt. Lett. **23**, 543–545 (1998)

11.19 R.M. Macfarlane, M.J. Dejneka: Spectral hole burning in thulium-doped glass ceramics, Opt. Lett. **26**, 429–431 (2001)

11.20 H. Ebendorff-Heidepriem: Laser writing of waveguides in photosensitive glasses, Opt. Mater. **25**, 109–115 (2004)

11.21 L.B. Glebov: Photosensitive holographic glass—New approach to creation of high power lasers, Phys. Chem. Glasses **48**, 123–128 (2007)

11.22 J. Lumeau, L. Glebova, V. Golubkov, E.D. Zanotto, L.B. Glebov: Origin of crystallization-induced refractive index changes in photo-thermo-refractive glass, Opt. Mater. **32**, 139–146 (2009)

11.23 K.H.M. Tantawi, J. Oates, R. Kamali-Sarvestani, N. Bergquist, J.D. Williams: Processing of photosensitive APEX glass structures with smooth and transparent sidewalls, J. Micromech. Microeng. **21**, 017001 (2011)

11.24 D. Du, X. Liu, G. Korn, J. Squier, G. Mourou: Laser-induced breakdown by impact ionization in SiO_2

with pulse widths from 7 ns to 150 fs, Appl. Phys. Lett. **64**, 3071–3073 (1994)
11.25 D. Strickland, G. Mourou: Compression of amplified chirped optical pulses, Opt. Commun. **56**, 219–221 (1985)
11.26 M.D. Perry, G. Mourou: Terawatt to petawatt subpicosecond lasers, Science **264**, 917–924 (1994)
11.27 K. Sugioka, Y. Cheng: Ultrafast lasers–Reliable tools for advanced materials processing, Light Sci. Appl. **3**, e149 (2014)
11.28 W. Sibbett, A.A. Lagatsky, C.T.A. Brown: The development and application of femtosecond laser systems, Opt. Express **20**, 6989–7001 (2012)
11.29 B.C. Stuart, M.D. Feit, A.M. Rubenchik, B.W. Shore, M.D. Perry: Laser-induced damage in dielectrics with nanosecond to subpicosecond pulses, Phys. Rev. Lett. **74**, 2248–2251 (1995)
11.30 N. Bloembergen: A brief history of light breakdown, J. Nonlinear Opt. Phys. Mater. **6**, 377–385 (1997)
11.31 B.C. Stuart, M.D. Feit, S. Herman, A.M. Rubenchik, B.W. Shore, M.D. Perry: Nanosecond-to-femtosecond laser-induced breakdown in dielectrics, Phys. Rev. B **53**, 1749–1761 (1996)
11.32 B.N. Chichkov, C. Momma, S. Nolte, F. von Alvensleben, A. Tünnermann: Femtosecond, picosecond and nanosecond laser ablation of solids, Appl. Phys. A **63**, 109–115 (1996)
11.33 O.M. Efimov, L.B. Glebov, S. Grantham, M. Richardson: Photoionization of silicate glasses exposed to IR femtosecond pulses, J. Non-Cryst. Solids **253**, 58–67 (1999)
11.34 S.K. Sundaram, E. Mazur: Inducing and probing non-thermal transitions in semiconductors using femtosecond laser pulses, Nat. Mater. **1**, 217–224 (2002)
11.35 M. Sakakura, M. Shimizu, Y. Shimotsuma, K. Miura, K. Hirao: Temperature distribution and modification mechanism inside glass with heat accumulation during 250 kHz irradiation of femtosecond laser pulses, Appl. Phys. Lett. **93**, 231112 (2008)
11.36 R.W. Boyd: *Nonlinear Optics* (Academic, San Diego 2008)
11.37 S. Kawata, H.-B. Sun, T. Tanaka, K. Takada: Finer features for functional microdevices, Nature **412**, 697–698 (2001)
11.38 J. Kasparian, J.-P. Wolf: Physics and applications of atmospheric nonlinear optics and filamentation, Opt. Express **16**, 466–493 (2008)
11.39 Q. Sun, H. Jiang, Y. Liu, Y. Zhou, H. Yang, Q. Gong: Effect of spherical aberration on the propagation of a tightly focused femtosecond laser pulse inside fused silica, J. Optics A **7**, 655–659 (2005)
11.40 A. Marcinkevičius, V. Mizeikis, S. Juodkazis, S. Matsuo, H. Misawa: Effect of refractive index-mismatch on laser microfabrication in silica glass, Appl. Phys. A **76**, 257–260 (2003)
11.41 M. Shimizu, M. Sakakura, M. Ohnishi, Y. Shimotsuma, T. Nakaya, K. Miura, K. Hirao: Mechanism of heat-modification inside a glass after irradiation with high-repetition rate femtosecond laser pulses, J. Appl. Phys. **108**, 073533 (2010)
11.42 M. Gu, D. Day, O. Nakamura, S. Kawata: Three-dimensional coherent transfer function for reflection confocal microscopy in the presence of refractive-index mismatch, J. Opt. Soc. Am. A **18**, 2002–2008 (2001)
11.43 C.W. Carr, H.B. Radousky, A.M. Rubenchik, M.D. Feit, S.G. Demos: Localized dynamics during laser-induced damage in optical materials, Phys. Rev. Lett. **92**, 087401 (2004)
11.44 E.G. Gamaly, S. Juodkazis, K. Nishimura, H. Misawa, B. Luther-Davies, L. Hallo, P. Nicolai, V.T. Tikhonchuk: Laser-matter interaction in the bulk of a transparent solid: Confined microexplosion and void formation, Phys. Rev. B **73**, 214101 (2006)
11.45 S.M. Eaton, H. Zhang, P.R. Herman, F. Yoshino, L. Shah, J. Bovatsek, A.Y. Arai: Heat accumulation effects in femtosecond laser-written waveguides with variable repetition rate, Opt. Express **13**, 4708–4716 (2005)
11.46 H. Zhang, S.M. Eaton, J. Li, P.R. Herman: Heat accumulation during high repetition rate ultrafast laser interaction: Waveguide writing in borosilicate glass, J. Phys. Conf. Ser. **59**, 682–686 (2007)
11.47 Y. Shimotsuma, K. Miura, M. Sakakura, S. Kanehira, K. Hirao: Formation of silicon structures in silicate glass by femtosecond laser, Proc. SPIE **6458**, 64580L (2007)
11.48 K. Miura, J. Qiu, T. Mitsuyu, K. Hirao: Space-selective growth of frequency-conversion crystals in glasses with ultrashort infrared laser pulses, Opt. Lett. **25**, 408–410 (2000)
11.49 S. Kanehira, K. Miura, K. Hirao: Ion exchange in glass using femtosecond laser irradiation, Appl. Phys. Lett. **93**, 023112 (2008)
11.50 Y. Liu, B. Zhu, L. Wang, J. Qiu, Y. Dai, H. Ma: Femtosecond laser induced coordination transformation and migration of ions in sodium borate glasses, Appl. Phys. Lett. **92**, 121113 (2008)
11.51 M. Shimizu, M. Sakakura, S. Kanehira, M. Nishi, Y. Shimotsuma, K. Hirao, K. Miura: Formation mechanism of element distribution in glass under femtosecond laser irradiation, Opt. Lett. **36**, 2161–2163 (2011)
11.52 M. Sakakura, M. Terazima, Y. Shimotsuma, K. Miura, K. Hirao: Heating and rapid cooling of bulk glass after photoexcitation by a focused femtosecond laser pulse, Opt. Express **15**, 16800–16807 (2007)
11.53 M. Shimizu, K. Miura, M. Sakakura, M. Nishi, Y. Shimotsuma, S. Kanehira, T. Nakaya, K. Hirao: Space-selective phase separation inside a glass by controlling compositional distribution with femtosecond-laser irradiation, Appl. Phys. A **100**, 1001–1005 (2010)
11.54 B.R. Wheaton, A.G. Clare: Evaluation of phase separation in glasses with the use of atomic force microscopy, J. Non-Cryst. Solids **353**, 4767–4778 (2007)

11.55 A. Hodroj, P. Simon, P. Florian, M.-H. Chopinet, Y. Vaills: Phase separation and spatial morphology in sodium silicate glasses by AFM, light scattering and NMR, J. Am. Ceram. Soc. **96**, 2454–2460 (2013)

11.56 W. Haller, D.H. Blackburn, J.H. Simmons: Miscibility gaps in alkali-silicate binaries—Data and thermodynamic interpretation, J. Am. Ceram. Soc. **57**, 120–126 (1974)

11.57 W. Haller: Rearrangement kinetics of the liquid–liquid immiscible microphases in alkali borosilicate melts, J. Chem. Phys. **42**, 686–693 (1965)

11.58 Y. Shimotsuma, K. Hirao, J. Qiu, K. Miura: Nanofabrication in transparent materials with a femtosecond pulse laser, J. Non-Cryst. Solids **352**, 646–656 (2006)

11.59 A. Nukui, T. Taniguchi, M. Miyata: In situ high-temperature x-ray observation of structural changes of tellurite glasses with p-block oxides-ZnO-TeO_2 glasses, J. Non-Cryst. Solids **293–295**, 255–260 (2001)

11.60 A. Mirgorodski, M. Colas-Dutreilh, M. Smirnov, T. Merle-Méjean, R. El-Mallawany, P. Thomas: Structural peculiarities and Raman spectra of TeO_2/WO_3 based glasses: A fresh look at the problem, J. Solid State Chem. **190**, 45–51 (2012)

11.61 A. Stone, H. Jain, V. Dierolf, M. Sakakura, Y. Shimotsuma, K. Miura, K. Hirao, J. Lapointe, R. Kashyap: Direct laser-writing of ferroelectric single-crystal waveguide architectures in glass for 3-D integrated optics, Sci. Rep. **5**, 10391 (2015)

11.62 A. Stone, H. Jain, V. Dierolf, M. Sakakura, Y. Shimotsuma, K. Miura, K. Hirao: Multilayer aberration correction for depth-independent 3-D crystal growth in glass by femtosecond laser heating, J. Opt. Soc. Am. B **30**, 1234–1240 (2013)

11.63 Y. Shimotsuma, K. Hirao, P.G. Kazansky, J. Qiu: Three-dimensional micro- and nano-fabrication in transparent materials by femtosecond laser, Jpn. J. Appl. Phys. **44**, 4735–4748 (2005)

11.64 J. Qiu, C. Zhu, T. Nakaya, J. Si, K. Kojima, F. Ogura, K. Hirao: Space-selective valence state manipulation of transition metal ions inside glasses by a femtosecond laser, Appl. Phys. Lett. **79**, 3567–3569 (2001)

11.65 S.P. Singh, A. Kumar: Absorption spectrum of Mn^{3+} and redox equilibria of iron and manganese in sodium silicate glass, Phys. Chem. Glasses **32**, 61–66 (1992)

11.66 R. Yokota: Color centers in alkali silicate and borate glasses, Phys. Rev. **95**, 1145–1148 (1954)

11.67 R.R. Alfano, S.L. Shapiro: Emission in the region 4000 to 7000 Å via four-photon coupling in glass, Phys. Rev. Lett. **24**, 584–587 (1970)

11.68 J. Qiu, K. Kojima, K. Miura, T. Mitsuyu, K. Hirao: Infrared femtosecond laser pulse-induced permanent reduction of Eu^{3+} to Eu^{2+} in a fluorozirconate glass, Opt. Lett. **24**, 786–788 (1999)

11.69 Y. Miyamoto, Y. Takei, H. Nanto, T. Kurobori, A. Konnai, T. Yanagida, A. Yoshikawa, Y. Shimotsuma, M. Sakakura, K. Miura, K. Hirao, Y. Nagashima, T. Yamamoto: Radiophotoluminescence from silver-doped phosphate glass, Radiat. Meas. **46**, 1480–1483 (2011)

11.70 J. Qiu: Femtosecond laser-induced microstructures in glasses and applications in micro-optics, Chem. Rec. **4**, 50–58 (2004)

11.71 R. Yokota, H. Imagawa: Radiophotoluminescent centers in silver-activated phosphate glass, J. Phys. Soc. Jpn. **23**, 1038–1047 (1969)

11.72 T. Ikegami: Read-out system for glass dosemeters using nitrogen gas laser, Hoshasen **17**, 10–17 (1991)

11.73 E. Piesch, B. Burgkhardt: Photoluminescence dosimetry: The alternative in personal monitoring, Radioprotection **29**, 39–67 (1994)

11.74 K. Nomura, T. Ikegami, N. Juto: Development of dosimeters for personal monitoring. I. Radiophoto-luminescent glass dosimeter, Radioisotopes **51**, 85–95 (2002)

11.75 Y. Miyamoto, T. Yamamoto, K. Kinoshita, S. Koyama, Y. Takei, H. Nanto, Y. Shimotsuma, M. Sakakura, K. Miura, K. Hirao: Emission mechanism of radiophotoluminescence in Ag-doped phosphate glass, Radiat. Meas. **45**, 546–549 (2010)

11.76 J.A. Perry: *RPL Dosimetry, Radiophotoluminescence in Health Physics* (Adam Hilger, Bristol 1987)

11.77 S.-M. Hsua, H.-W. Yang, T.-C. Yeh, W.-L. Hsu, C.-H. Wu, C.-C. Lu, W.-L. Chen, D.Y.C. Huang: Synthesis and physical characteristics of radiophotoluminescent glass dosimeters, Radiat. Meas. **42**, 621–624 (2007)

11.78 R. Yokota, H. Imagawa: Radiophotoluminescent centers in silver-activated phosphate glass, J. Phys. Soc. Jpn. **23**, 1038–1048 (1967)

11.79 D.L. Griscom, E.J. Friebele, K.J. Long: Fundamental defect centers in glass: Electron spin resonance and optical absorption studies of irradiated phosphorus-doped silica glass and optical fibers, J. Appl. Phys. **54**, 3743–3762 (1983)

11.80 K.M. Davis, K. Miura, N. Sugimoto, K. Hirao: Writing waveguides in glass with a femtosecond laser, Opt. Lett. **21**, 1729–1731 (1996)

11.81 C.B. Schaffer, A. Brodeur, E. Mazur: Laser-induced breakdown and damage in bulk transparent materials induced by tightly-focused femtosecond laser pulses, Meas. Sci. Technol. **12**, 1784–1794 (2001)

11.82 P.G. Kazansky, Y. Shimotsuma: Self-assembled sub-wavelength structures and form birefringence created by femtosecond laser writing in glass: Properties and applications, J. Ceram. Soc. Jpn. **116**, 1052–1062 (2008)

11.83 Y. Shimotsuma, M. Sakakura, K. Miura: Manipulation of optical anisotropy in silica glass, Opt. Mater. Express **1**, 803–815 (2011)

11.84 J.W. Chan, T.R. Huser, S.H. Risbud, D.M. Krol: Modification of the fused silica glass network associated with waveguide fabrication using femtosecond laser pulses, Appl. Phys. A **76**, 367–372 (2003)

11.85 W.J. Reichman, J.W. Chan, C.W. Smelser, S.J. Mihailov, D.M. Krol: Spectroscopic characterization of different femtosecond laser modification

regimes in fused silica, J. Opt. Soc. Am. B **24**, 1627–1632 (2007)
11.86 K. Miura, J. Qiu, H. Inouye, T. Mitsuyu, K. Hirao: Photowritten optical waveguides in various glasses with ultrashort laser pulses, Appl. Phys. Lett. **71**, 3329–3331 (1997)
11.87 G. Cerullo, R. Osellame, S. Taccheo, M. Marangoni, D. Polli, R. Ramponi, P. Laporta, S.D. Silverstri: Femtosecond micromachining of symmetric waveguides at 1.5 m by astigmatic beam focusing, Opt. Lett. **27**, 1938–1940 (2002)
11.88 M. Sakakura, M. Terazima, Y. Shimotsuma, K. Miura, K. Hirao: Thermal and shock induced modification inside a silica glass by focused femtosecond laser pulse, J. Appl. Phys. **109**, 023503 (2011)
11.89 E. Glezer, E. Mazur: Ultrafast-laser driven microexplosions in transparent materials, Appl. Phys. Lett. **71**, 882–884 (1997)
11.90 H. Sun, Y. Xu, S. Juodkazis, K. Sun, M. Watanabe, S. Matsuo, H. Misawa, J. Nishii: Arbitrary-lattice photonic crystals created by multiphoton microfabrication, Opt. Lett. **26**, 325–327 (2001)
11.91 L. Sudrie, A. Couairon, M. Franco, B. Lamouroux, B. Prade, S. Tzortzakis, A. Mysyrowicz: Femtosecond laser induced damages and filamentary propagation in fused silica, Phys. Rev. Lett. **89**, 186601 (2002)
11.92 A. Couairon, L. Sudrie, M. Franco, B. Prade, A. Mysyrowicz: Filamentation and damage in fused silica induced by tightly focused femtosecond laser pulses, Phys. Rev. B **71**, 125435 (2005)
11.93 L. Sudrie, M. Franco, B. Prade, A. Mysyrowicz: Writing of permanent birefringent microlayers in bulk fused silica with femtosecond laser pulses, Opt. Commun. **171**, 279–284 (1996)
11.94 L. Sudrie, M. Franco, B. Prade, A. Mysyrowicz: Study of damage in fused silica induced by ultrashort IR laser pulses, Opt. Commun. **191**, 333–333 (2001)
11.95 P.G. Kazansky, H. Inouye, T. Mitsuyu, K. Miura, J. Qiu, K. Hirao, F. Starrost: Anomalous anisotropic light scattering in Ge-doped silica glass, Phys. Rev. Lett. **82**, 2199–2202 (1999)
11.96 Y. Shimotsuma, P.G. Kazansky, J. Qiu, K. Hirao: Self-organized nanogratings in glass irradiated by ultrashort light pulses, Phys. Rev. Lett. **24**, 2474051 (2003)
11.97 Y. Shimotsuma, K. Hirao, J. Qiu, P.G. Kazansky: Nano-modification inside transparent materials by femtosecond laser single beam, Mod. Phys. Lett. B **19**, 225–238 (2005)
11.98 E. Bricchi, B.G. Klappauf, P.G. Kazansky: Form birefringence and negative index change created by femtosecond direct writing in transparent materials, Opt. Lett. **29**, 119–121 (2004)
11.99 J.D. Mills, P.G. Kazansky, E. Bricchi, J.J. Baumberg: Embedded anisotropic microreflectors by femtosecond-laser nanomachining, Appl. Phys. Lett. **81**, 196–198 (2002)
11.100 C. Hnatovsky, R.S. Taylor, P.P. Rajeev, E. Simova, V.R. Bhardwaj, D.M. Rayner, P.B. Corkum: Pulse duration dependence of femtosecond-laser-fabricated nanogratings in fused silica, Appl. Phys. Lett. **87**, 014104 (2005)
11.101 Y. Shimotsuma, M. Sakakura, P.G. Kazansky, M. Beresna, J. Qiu, K. Miura, K. Hirao: Ultrafast manipulation of self-assembled form birefringence in glass, Adv. Mater. **22**, 4039–4043 (2010)
11.102 M. Sakakura, M. Terazima: Initial temporal and spatial changes of the refractive index induced by focused femtosecond pulsed laser irradiation inside a glass, Phys. Rev. B **71**, 024113 (2005)
11.103 M. Sakakura, M. Terazima, Y. Shimotsuma, K. Miura, K. Hirao: Observation of pressure wave generated by focusing a femtosecond laser pulse inside a glass, Opt. Express **15**, 5674–5686 (2007)
11.104 A. Mermillod-Blondin, I.M. Burakov, Y.P. Meshcheryakov, N.M. Bulgakova, E. Audouard, A. Rosenfeld, A. Husakou, I.V. Hertel, R. Stoian: Flipping the sign of refractive index changes in ultrafast and temporally shaped laser-irradiated borosilicate crown optical glass at high repetition rates, Phys. Rev. B **77**, 104205 (2008)
11.105 R. Brückner: Properties and structure of vitreous silica. I, J. Non-Cryst. Solids **5**, 123–175 (1970)
11.106 J.E. Shelby: Density of vitreous silica, J. Non-Cryst. Solids **349**, 331–336 (2004)
11.107 M. Terazima: Ultrafast transient Kerr lens in solution detected by the dual-beam thermal-lens method, Opt. Lett. **20**, 25–27 (1995)
11.108 P. Martin, S. Guizard, P. Daguzan, G. Petite, P. D'Oliveira, P. Meynadier, M. Perdrix: Subpicosecond study of carrier trapping dynamics in wide-band-gap crystals, Phys. Rev. B **55**, 5799–5810 (1997)
11.109 L. Skuja: The origin of the intrinsic 1.9 eV luminescence band in glassy SiO_2, J. Non-Cryst. Solids **179**, 51–69 (1994)
11.110 I. Daniel, P. Gillet, B.T. Poe, P.F. McMillan: In-situ high-temperature Raman spectroscopic studies of aluminosilicate liquids, Phys. Chem. Miner. **22**, 74–86 (1995)
11.111 P.F. McMillan, B. Piriou, R. Couty: A Raman study of pressure-densified vitreous silica, J. Chem. Phys. **81**, 4234–4236 (1984)
11.112 M. Okuno, B. Reynard, M. Shimada, Y. Syono, C. Willaime: A Raman spectroscopic study of shock-wave densification of vitreous silica, Phys. Chem. Miner. **26**, 304–311 (1999)
11.113 A. Vogel, J. Noack, G. Huttman, G. Paltauf: Mechanisms of femtosecond laser nanosurgery of cells and tissues, Appl. Phys. B **81**, 1015–1047 (2005)
11.114 K. Mishchik, C. D'Amico, P.K. Velpula, C. Mauclair, A. Boukenter, Y. Ouerdane, R. Stoian: Ultrafast laser induced electronic and structural modifications in bulk fused silica, J. Appl. Phys. **114**, 133502 (2013)
11.115 M. Born, E. Wolf: *Principles of Optics* (Cambridge Univ. Press, Cambridge 1999)
11.116 L.D. Landau, E.M. Lifshitz: *Theory of Elasticity* (Pergamon, New York 1986)
11.117 L. Shah, J. Tawney, M. Richardson, K. Richardson: Self-focusing during femtosecond micromachin-

ing of silicate glasses, IEEE J. Quantum Electron. **40**, 57–68 (2004)
11.118 S.-H. Cho, H. Kumagai, I. Yokota, K. Midorikawa, M. Obara: Observation of self-channeled plasma formation and bulk modification in optical fibers using high-intensity femtosecond laser, Jpn. J. Appl. Phys. **37**, L737–L739 (1998)
11.119 V. Dimitrov, T. Komatsu: Polarizability, basicity and chemical bonding of single and multicomponent oxide glasses, J. Chem. Technol. Metall. **50**, 387–396 (2015)
11.120 S.-H. Kim, T. Yoko, S. Sakka: Linear and nonlinear optical properties of TeO_2 glass, J. Am. Ceram. Soc. **76**, 2486–2490 (1993)
11.121 V. Dimitrov, S. Sakka: Linear and nonlinear optical properties of simple oxides. II, J. Appl. Phys. **79**, 1741–1745 (1993)
11.122 P.G. Kazansky, E. Bricchi, Y. Shimotsuma, K. Hirao: Self-assembled nanostructures and two-plasmon decay in femtosecond processing of transparent materials. In: *Conf. Lasers Electro-Opt., CLEO, Baltimore* (2007) pp. U1–2
11.123 V.R. Bhardwaj, E. Simova, P.P. Rajeev, C. Hnatovsky, R.S. Taylor, D.M. Rayner, P.B. Corkum: Optically produced arrays of planar nanostructures inside fused silica, Phys. Rev. Lett. **96**, 057404 (2006)
11.124 P. Rajeev, M. Gertsvolf, C. Hnatovsky, E. Simova, R. Taylor, P. Corkum, D. Rayner, V. Bhardwaj: Transient nanoplasmonics inside dielectrics, J. Phys. B **40**, S273–S282 (2007)
11.125 M. Beresna, M. Gecevicius, P.G. Kazansky, T. Taylor, A.V. Kavokin: Exciton mediated self-organization in glass driven by ultrashort light pulses, Appl. Phys. Lett. **101**, 053120 (2012)
11.126 A. Brodeur, S.L. Chin: Ultrafast white-light continuum generation and self-focusing in transparent condensed media, J. Opt. Soc. Am. B **16**, 637–650 (1999)
11.127 B.-T.V. Vu, O.L. Landen, A. Szoke: Time-resolved probing of femtosecond-laser-produced plasmas in transparent solids by electron thermal transport, Phys. Plasmas **2**, 476–485 (1995)
11.128 I.M. Burakov, N.M. Bulgakova, R. Stoian, A. Mermillod-Blondin, E. Audouard, A. Rosenfeld, A. Husakou, I.V. Hertel: Spatial distribution of refractive index variations induced in bulk fused silica by single ultrashort and short laser pulses, J. Appl. Phys. **101**, 043506 (2007)
11.129 D.G. Papazoglou, I. Zergioti, S. Tzortzakis: Plasma strings from ultraviolet laser filaments drive permanent structural modifications in fused silica, Opt. Lett. **32**, 2055–2057 (2007)
11.130 Y. Liao, W. Pan, Y. Cui, L. Qiao, Y. Bellouard, K. Sugioka, Y. Cheng: Formation of in-volume nanogratings with sub-100-nm periods in glass by femtosecond laser irradiation, Opt. Lett. **40**, 3623–3626 (2015)
11.131 Y. Dai, A. Patel, J. Song, M. Beresna, P.G. Kazansky: Void-nanograting transition by ultrashort laser pulse irradiation in silica glass, Opt. Express **24**, 19344–19353 (2016)
11.132 P.K. Singh, A. Adak, A.D. Lad, G. Chatterjee, P. Brijesh, G.R. Kumar: Controlling two plasmon decay instability in intense femtosecond laser driven plasmas, Phys. Plasmas **22**, 113114 (2015)
11.133 K. Estabrook, W.L. Kruer, B.F. Lasinski: Heating by Raman backscatter and forward scatter, Phys. Rev. Lett. **45**, 1399–1403 (1980)
11.134 T.J.M. Boyd: The trouble with laser-plasma interactions, Plasma Phys. Control. Fusion **28**, 1887–1903 (1986)
11.135 M. Watanabe, S. Juodkazis, J. Nishii, S. Matsuo, H. Mizawa: Microfabrication by a high fluence femtosecond exposure: Mechanism and applications, Proc. SPIE **4637**, 159 (2002)
11.136 A. Patel, M. Gecevičius, R. Drevinskas, M. Beresna, P.G. Kazansky: 3/2 harmonic generation—The clue to the mechanism of ultrafast laser nanostructuring. In: *CLEO: 2013 OSA Technical Digest* (Optical Society of America, Washington DC 2013), CM2M.2
11.137 R. Taylor, C. Hnatovsky, E. Simova: Applications of femtosecond laser induced self-organized planar nanocracks inside fused silica glass, Laser Photonics Rev. **2**, 26–46 (2008)
11.138 P.P. Rajeev, M. Gerstvolf, E. Simova, C. Hnatovsky, R.S. Taylor, D.M. Rayner, P.B. Corkum: Memory in nonlinear ionization of transparent solids, Phys. Rev. Lett. **97**, 253001 (2006)
11.139 R. Buividas, L. Rosa, R. Sliupas, T. Kudrius, G. Slekys, V. Datsyuk, S. Juodkazis: Mechanism of fine ripple formation on surfaces of (semi)transparent materials via a half-wavelength cavity feedback, Nanotechnology **22**, 055304 (2011)
11.140 W. Yang, E. Bricchi, P.G. Kazansky, J. Bovatsek, A.Y. Arai: Self-assembled periodic sub-wavelength structures by femtosecond laser direct writing, Opt. Express **14**, 10117–10124 (2006)
11.141 S. Richter, M. Heinrich, S. Döring, A. Tünnermann, S. Nolte: Nanogratings in fused silica: Formation, control, and applications, J. Laser Appl. **24**, 042008 (2012)
11.142 M. Lancry, B. Poumellec, J. Canning, K. Cook, J.Ä. Poulin, F. Brisset: Ultrafast nanoporous silica formation driven by femtosecond laser irradiation, Laser Photonics Rev. **7**, 953–962 (2013)
11.143 S. Richter, A. Plech, M. Steinert, M. Heinrich, S. Döring, F. Zimmermann, U. Peschel, E.B. Kley, A. Tünnermann, S. Nolte: On the fundamental structure of femtosecond laser-induced nanogratings, Laser Photonics Rev. **6**, 787–792 (2012)
11.144 Y. Shimotsuma, K. Miura, K. Hirao: Nanomodification of glass using fs laser, Int. J. Appl. Glass Sci. **4**, 182–191 (2013)
11.145 M. Lancry, J. Canning, K. Cook, M. Heili, D.R. Neuville, B. Poumellec: Nanoscale femtosecond laser milling and control of nanoporosity in the normal and anomalous regimes of GeO_2-SiO_2 glasses, Opt. Mater. Express **6**, 321–330 (2016)
11.146 V. Oliveira, S.P. Sharma, P. Herrero, R. Vilar: Transformations induced in bulk amorphous silica by

ultrafast laser direct writing, Opt. Lett. **38**, 4950–4953 (2013)
11.147 S. Richter, C. Miese, S. Döring, F. Zimmermann, M.J. Withford, A. Tünnermann, S. Nolte: Laser induced nanogratings beyond fused silica–periodic nanostructures in borosilicate glasses and ULE, Opt. Mater. Express **3**, 1161–1166 (2013)
11.148 F. Zimmermann, A. Plech, S. Richter, A. Tünnermann, S. Nolte: Ultrashort laser pulse induced nanogratings in borosilicate glass, Appl. Phys. Lett. **104**, 211107 (2014)
11.149 A. Paleari, E. Franchina, N. Chiodini, A. Lauria, E. Bricchi, P.G. Kazansky: SnO_2 nanoparticles in silica: Nanosized tools for femtosecond-laser machining of refractive index patterns, Appl. Phys. Lett. **88**, 131912 (2006)
11.150 T. Asai, Y. Shimotsuma, T. Kurita, A. Murata, S. Kubota, M. Sakakura, K. Miura, F. Brisset, B. Poumellec, M. Lancry: Systematic control of structural changes in GeO_2 glass induced by femtosecond laser direct writing, J. Am. Ceram. Soc. **98**, 1471–1477 (2015)
11.151 J. Canning, M. Lancry, K. Cook, A. Weickman, F. Brisset, B. Poumellec: Anatomy of a femtosecond laser processed silica waveguide, Opt. Mater. Express **1**, 998–1008 (2011)
11.152 L. Bressel, D. de Ligny, E.G. Gamaly, A.V. Rode, S. Juodkazis: Observation of O_2 inside voids formed in GeO_2 glass by tightly-focused fs-laser pulses, Opt. Mater. Express **1**, 1150–1158 (2011)
11.153 M.M. Braun, L. Pilon: Effective optical properties of non-absorbing nanoporous thin films, Thin Solid Films **496**, 505–514 (2006)
11.154 M. Rothschild, D.J. Ehrlich, D.C. Shaver: Effects of excimer laser irradiation on the transmission, index of refraction, and density of ultraviolet grade fused silica, Appl. Phys. Lett. **55**, 1276–1278 (1989)
11.155 M.K. Schurman, M. Tomozawa: Equilibrium oxygen vacancy concentrations and oxidant diffusion in germania, silica, and germania-silica glasses, J. Non-Cryst. Solids **202**, 93–106 (1996)
11.156 J. Zhang, M. Gecevičius, M. Beresna, P.G. Kazansky: Seemingly unlimited lifetime data storage in nanostructured glass, Phys. Rev. Lett. **112**, 033901 (2014)
11.157 Y. Shimotsuma, S. Kubota, A. Murata, T. Kurita, M. Sakakura, K. Miura, M. Lancry, B. Poumellec: Tunability of form birefringence induced by femtosecond laser irradiation in anion-doped silica glass, J. Am. Ceram. Soc. **100**, 3912–3919 (2017)
11.158 K. Sugioka, M. Iida, H. Takai, K. Micorikawa: Efficient microwelding of glass substrates by ultrafast laser irradiation using a double-pulse train, Opt. Lett. **36**, 2734–2736 (2011)
11.159 A. Mouskeftaras, S. Guizard, N. Fedorov, S. Klimentov: Mechanisms of femtosecond laser ablation of dielectrics revealed by double pump-probe experiment, Appl. Phys. A **110**, 709–715 (2013)
11.160 P.G. Kazansky, W. Yang, E. Bricchi, J. Bovatsek, A. Arai, Y. Shimotsuma, K. Miura, K. Hirao: "Quill" writing with ultrashort light pulses in transparent materials, Appl. Phys. Lett. **90**, 151120 (2007)
11.161 A. Murata, Y. Shimotsuma, M. Sakakura, K. Miura: Control of periodic nanostructure embedded in SiO_2 glass under femtosecond double-pulse irradiation, J. Laser Micro/Nanoeng. **11**, 95–99 (2016)
11.162 S. Richter, F. Jia, M. Heinrich, S. Döring, U. Peschel, A. Tünnermann, S. Nolte: The role of self-trapped excitons and defects in the formation of nanogratings in fused silica, Opt. Lett. **37**, 482–484 (2012)
11.163 D.H. Goldstein: *Polarized Light* (CRC, New York 2010)
11.164 V.G. Dmitriev, G.G. Gurzadyan, D.N. Nikogosyan, H.K.V. Lotsch: *Handbook of Nonlinear Optical Crystals* (Springer, Berlin 1999)
11.165 A.V. Kolobov, J. Tominaga: *Chalcogenides: Metastability and Phase Change Phenomena* (Springer, Berlin 2012)
11.166 W. Yang, P.G. Kazansky, Y.P. Svirko: Non-reciprocal ultrafast laser writing, Nat. Photonics **2**, 99–104 (2008)
11.167 W. Yang, P.G. Kazansky, Y. Shimotsuma, M. Sakakura, K. Miura, K. Hirao: Ultrashort-pulse laser calligraphy, Appl. Phys. Lett. **93**, 171109 (2008)
11.168 D.N. Vitek, E. Block, Y. Bellouard, D.E. Adams, S. Backus, D. Kleinfeld, C.G. Durfee, J.A. Squier: Spatio-temporally focused femtosecond laser pulses for nonreciprocal writing in optically transparent materials, Opt. Express **18**, 24673–24678 (2010)
11.169 P.G. Kazansky, Y. Shimotsuma, M. Sakakura, M. Beresna, M. Gecevičius, Y. Svirko, S. Akturk, J. Qiu, K. Miura, K. Hirao: Photosensitivity control of an isotropic medium through polarization of light pulses with tilted intensity front, Opt. Express **19**, 20657–20664 (2011)
11.170 A.G. Kalampounias, S.N. Yannopoulos, G.N. Papatheodorou: Temperature-induced structural changes in glassy, supercooled, and molten silica from 77 to 2150 K, J. Chem. Phys. **124**, 014504 (2006)
11.171 N. Shimodaira, K. Saito, N. Hiramitsu, S. Matsushita, A.J. Ikushima: Effects of fictive temperature and halogen doping on the boson peak in silica glass, Phys. Rev. B **71**, 024209 (2005)
11.172 P. McMillan, B. Piriou, A. Navrotsky: A Raman spectroscopic study of glasses along the joins silica–calcium aluminate, silica–sodium aluminate, and silica–potassium aluminate, Geochim. Cosmochim. Acta **46**, 2021–2037 (1982)
11.173 S. Akturk, X. Gu, E. Zeek, R. Trebino: Pulse-front tilt caused by spatial and temporal chirp, Opt. Express **12**, 4399–4410 (2004)
11.174 S. Akturk, X. Gu, P. Gabolde, R. Trebino: The general theory of first-order spatio-temporal distortions of Gaussian pulses and beams, Opt. Express **13**, 8642–8661 (2005)

Yasuhiko Shimotsuma

Dept. of Materials Chemistry
Kyoto University
Kyoto, Japan
yshimo@func.mc.kyoto-u.ac.jp

Yasuhiko Shimotsuma is currently an Associate Professor at the Department of Material Chemistry, Kyoto University. He was a Research Scientist at the Division for Components & Devices of Kyocera Corporation (1996-2004) before receiving his PhD from Kyoto University in 2005. His current research area is understanding the physics of light-matter interaction.

Masaaki Sakakura

Optoelectronics Research Centre
University of Southampton
Southampton, UK
m.sakakura@soton.ac.uk

Masaaki Sakakura is currently a Researcher at the Optoelectronics Research Centre of the University of Southampton. He received his PhD from Kyoto University (2004) and has served as a JSPS Postdoctoral Research Fellow, JST Researcher and Program-Specific Associate Professor at Kyoto University (2005-2017). His current research focuses on femtosecond laser micromachining.

Masahiro Shimizu

Dept. of Materials Chemistry
Kyoto University
Kyoto, Japan
m.shimizu@func.mc.kyoto-u.ac.jp

Masahiro Shimizu is currently an Assistant Professor at the Department of Material Chemistry, Kyoto University, focusing on glass science. He received his PhD from Kyoto University (2012), served as JSPS Postdoctoral Research Fellow (2012-2013), and as a Visiting Researcher at Alfred University (2017).

Kiyotaka Miura

Dept. of Materials Chemistry
Kyoto University
Kyoto, Japan
kmiura@func.mc.kyoto-u.ac.jp

Kiyotaka Miura is currently a Professor at the Department of Material Chemistry, Kyoto University. He received his PhD from Kyoto University in 2002, while working as a Research Scientist for HOYA Corporation and Central Glass Corporation (1985-2005). He investigates photoinduced structures in glasses and functional devices using active glasses.

Kazuyuki Hirao

Dept. of Materials Chemistry
Kyoto University
Kyoto, Japan
hirao@bisco1.kuic.kyoto-u.ac.jp

Kazuyuki Hirao is a Professor at the Department of Material Chemistry, Kyoto University. He was a Postdoctoral Fellow at Rensselaer Polytechnic Institute and the Director of the Hirao Active Glass Project from 1994 to 1999. He received several awards including the Gottardi International Prize (1990) and the Morey International Prize (2002). In 2002, he became a Fellow of the American Ceramic Society.

Jianrong Qiu

Dept. of Materials Science & Engineering
Zhenjiang University
Hangzhou, China
qjr@zju.edu.cn

Jianrong Qiu is currently a Professor at the Department of Materials Science, Zhejiang University. He received his PhD from Okayama University in 1992 and was a Visiting Researcher of Cornell University from 1999 to 2000.He has received several awards including the Morey Award from the American Ceramic Society in 2015. His current research area is photonic materials.

Peter G. Kazansky

Optoelectronics Research Centre
University of Southampton
Southampton, UK
pgk@soton.ac.uk

Peter G. Kazansky is currently a Professor at the Department of Material Chemistry, Kyoto University. He received PhD from the General Physics Institute in 1985. He was awarded the Royal Society Fellowship at the ORC in 1992 and is a Fellow of the Optical Society of America. His current research focuses on the area of advanced photonic materials.